Structure of the trypanosome cyanide-insensitive alternative oxidase

Tomoo Shiba[a,1,2], Yasutoshi Kido[a,1,3], Kimitoshi Sakamoto[a,4], Daniel Ken Inaoka[a], Chiaki Tsuge[a], Ryoko Tatsumi[a], Gen Takahashi[b], Emmanuel Oluwadare Balogun[a,b,c], Takeshi Nara[d], Takashi Aoki[d], Teruki Honma[e], Akiko Tanaka[e], Masayuki Inoue[f], Shigeru Matsuoka[f], Hiroyuki Saimoto[g], Anthony L. Moore[h], Shigeharu Harada[b,5], and Kiyoshi Kita[a,5]

[a]Department of Biomedical Chemistry, Graduate School of Medicine, and [f]Graduate School of Pharmaceutical Sciences, The University of Tokyo, Tokyo 113-0033, Japan; [b]Department of Applied Biology, Graduate School of Science and Technology, Kyoto Institute of Technology, Kyoto 606-8585, Japan; [c]Department of Biochemistry, Ahmadu Bello University, Zaria 2222, Nigeria; [d]Department of Molecular and Cellular Parasitology, Juntendo University School of Medicine, Tokyo 113-8421, Japan; [e]Systems and Structural Biology Center, RIKEN, Tsurumi, Yokohama 230-0045, Japan; [g]Department of Chemistry and Biotechnology, Graduate School of Engineering, Tottori University, Tottori 680-8552, Japan; and [h]Biochemistry and Molecular Biology, School of Life Sciences, University of Sussex, Brighton BN1 9QG, United Kingdom

Edited[†] by John E. Walker, Medical Research Council Mitochondrial Biology Unit, Cambridge, United Kingdom, and approved February 11, 2013 (received for review October 23, 2012)

In addition to haem copper oxidases, all higher plants, some algae, yeasts, molds, metazoans, and pathogenic microorganisms such as *Trypanosoma brucei* contain an additional terminal oxidase, the cyanide-insensitive alternative oxidase (AOX). AOX is a diiron carboxylate protein that catalyzes the four-electron reduction of dioxygen to water by ubiquinol. In *T. brucei*, a parasite that causes human African sleeping sickness, AOX plays a critical role in the survival of the parasite in its bloodstream form. Because AOX is absent from mammals, this protein represents a unique and promising therapeutic target. Despite its bioenergetic and medical importance, however, structural features of any AOX are yet to be elucidated. Here we report crystal structures of the trypanosomal alternative oxidase in the absence and presence of ascofuranone derivatives. All structures reveal that the oxidase is a homodimer with the nonhaem diiron carboxylate active site buried within a four-helix bundle. Unusually, the active site is ligated solely by four glutamate residues in its oxidized inhibitor-free state; however, inhibitor binding induces the ligation of a histidine residue. A highly conserved Tyr220 is within 4 Å of the active site and is critical for catalytic activity. All structures also reveal that there are two hydrophobic cavities per monomer. Both inhibitors bind to one cavity within 4 Å and 5 Å of the active site and Tyr220, respectively. A second cavity interacts with the inhibitor-binding cavity at the diiron center. We suggest that both cavities bind ubiquinol and along with Tyr220 are required for the catalytic cycle for O_2 reduction.

diiron protein | neglected tropical diseases | monotopic membrane protein | drug target | ubiquinol oxidase

The alternative oxidase (AOX) is a nonprotonmotive ubiquinol oxidase catalyzing the four-electron reduction of dioxygen to water (1). The gene encoding this protein has been found in all higher plants, some algae, yeast, slime molds, free-living amoebae, eubacteria, nematodes, and some parasites including *Trypanosoma brucei* (2–5). *T. brucei* is a parasite that causes human African sleeping sickness and nagana in livestock and is transmitted by the tsetse fly (5). The development of chemotherapy and the continued search for new, unique therapeutic targets for African trypanosomiasis are urgently required, because current treatments, which are poorly targeted, have unacceptable side effects and efficacy (6).

The bloodstream form of *T. brucei* is equipped with a unique energy metabolism, namely an altered respiratory chain (5) and a modified ATP synthase (7). The parasites live as the bloodstream form in the mammalian host and as the procyclic form in the tsetse fly (5). The procyclic form of *T. brucei* contains a cytochrome-dependent respiratory chain in addition to an alternative oxidase, whereas within the bloodstream trypanosomes use the glycolytic pathway, localized in the glycosome, as their major source of ATP (5, 8). Once the parasites invade the mammalian host in the bloodstream, both the cytochrome respiratory pathway and oxidative phosphorylation disappear and are replaced by the trypanosomal alternative oxidase (TAO), which functions as the sole terminal oxidase to reoxidize NADH accumulated during glycolysis (5). Because NADH reoxidation is essential for parasite survival and mammalian hosts do not possess this protein, TAO is considered to be a unique target for antitrypanosomal drugs (9). Indeed, we have previously reported that the antibiotic ascofuranone (AF), isolated from the pathogenic fungus *Ascochyta viciae*, specifically inhibits the quinol oxidase activity of TAO at subnanomolar concentrations and rapidly kills the parasites (10). Furthermore, we have confirmed the chemotherapeutic efficacy of ascofuranone in vivo (11, 12).

Despite universal conservation of the gene encoding the AOX and diversified physiology (2), the molecular features of this protein have yet to be fully characterized. Current structural models predict that the AOX is an integral interfacial membrane protein that interacts with a single leaflet of the lipid bilayer and contains a nonhaem diiron carboxylate active site (1, 13, 14). This model is supported by extensive site-directed mutagenesis and spectroscopic studies (3, 15–20).

There are many proteins that belong to the diiron carboxylate protein family, and in each case they are characterized by the possession of two copies of the diiron binding motifs (21, 22). To date the majority of proteins within this family whose crystal structures have been determined are soluble proteins, and hence determination of a crystal structure of a member of the membrane-bound class is vital, because it would transformationally improve our understanding of the structure–function relationships of this functionally diverse family of proteins. In this paper we report on the crystal structure of the

Author contributions: T.S., Y.K., K.S., D.K.I., E.O.B., A.L.M., S.H., and K.K. designed research; T.S., Y.K., D.K.I., C.T., R.T., G.T., E.O.B., and H.S. performed research; K.S. and H.S. contributed new reagents/analytic tools; T.S., Y.K., G.T., T.N., T.A., T.H., A.T., M.I., and S.M. analyzed data; and T.S., Y.K., A.L.M., S.H., and K.K. wrote the paper.

The authors declare no conflict of interest.

[†]This Direct Submission article had a prearranged editor.

Data deposition: The atomic coordinates and structure factors have been deposited in the Protein Data Bank, www.pdb.org (PDB ID codes 3VV9 [trypanosomal alternative oxidase (TAO)], 3VVA [TAO-AF279OH complex], and 3W54 [TAO-colletochlorin B complex]).

[1]T.S. and Y.K. contributed equally to this work.

[2]Present address: Department of Applied Biology, Graduate School of Science and Technology, Kyoto Institute of Technology, Kyoto 606-8585, Japan.

[3]Present address: Division of International Health, Oita University Faculty of Medicine, Yufu, Oita 879-5593, Japan.

[4]Present address: Faculty of Agriculture and Life Science, Hirosaki University, Hirosaki 036-8561, Japan.

[5]To whom correspondence may be addressed. E-mail: harada@kit.ac.jp or kitak@m.u-tokyo.ac.jp.

This article contains supporting information online at www.pnas.org/lookup/suppl/doi:10.1073/pnas.1218386110/-/DCSupplemental.

oxidized form of the trypanosomal alternative oxidase at 2.85 Å. In addition to this very important milestone we also describe the structures of the active site of the enzyme in the presence of AF derivatives, AF2779OH and colletochlorin B (CCB), at 2.6 Å and 2.3 Å resolution, respectively. We believe that a detailed knowledge of the active site of the enzyme in the presence of such inhibitors will lead to a greater rational design of further potent and safer antitrypanosomal drugs.

Results and Discussion

Overall Structure of TAO. We have recently established protocols to prepare highly purified and stable TAO, which has enabled us to crystallize the enzyme (23, 24). The crystal structure of TAO determined at 2.85 Å resolution (*SI Appendix*, Table S1) contains four monomers per asymmetric unit that associate to form homodimers (Fig. 1*A* and *SI Appendix*, Fig. S1*A*). Each monomer, which lacks about 30 residues in both N- and C-terminal regions due to faint electron density, consists of a long N-terminal arm, six long α helices (α1–α6), and four short helices (S1–S4). The long helices are arranged in an antiparallel fashion with α2, α3, α5, and α6 forming a four-helix bundle that accommodates a diiron center, as widely observed in other diiron carboxylate proteins (1, 14) (*SI Appendix*, Fig. S2). Except for the N-terminal arm, each monomer is shaped as a compact cylinder (50 × 35 × 30 Å), and there are no significant structural differences among monomers in the asymmetric unit, as indicated by rms deviations (0.49~0.68 Å) for superimposed Cα positions of the six helices calculated between a pair of monomers. However, loops connecting adjacent helices show larger differences among monomers, resulting in somewhat larger rms deviations (0.67~0.88 Å) when calculated using all Cα atoms.

In the dimer, two monomers are related by a noncrystallographic twofold axis approximately perpendicular to the bundle (Fig. 1*A*). Helices α2, α3, and α4 of one monomer and α2*, α3*, and α4* of the other (asterisk denotes helix of a neighboring monomer) build a dimer interface, where six completely conserved residues (H138, L142, R143, R163, L166, and Q187) and 12 highly conserved residues (M131, M135, L139, S141, M145, R147, D148, L156, A159, M167, R180, and I183) are involved in the interaction between monomers (*SI Appendix*, Fig. S3), suggesting that a dimeric structure is common to all AOXs. In addition, the N-terminal arm (P31~R62) of one monomer extends into the other monomer (Fig. 1*A*), suggesting that the arm is important for dimerization. Upon dimerization, about 2,490 Å^2 of solvent-accessible surface (35% of the total dimer surface) is buried. A large hydrophobic region is visible on one side of the dimer surface that is formed by α1 and α4 plus the C-terminal region of α2 and the N-terminal region of α5 from both monomers (Fig. 1*B Left*). Because the opposite side of the dimer surface is relatively hydrophilic (Fig. 1*B Right*), we propose that the dimer is bound to the mitochondrial inner membrane via this hydrophobic region in an interfacial fashion, as originally suggested by Andersson and Nordlund (13). The membrane penetration depth of TAO, calculated by PPM web server (25), is 8.4 Å, roughly corresponding to the radius of a helix. In addition, basic residues (R106, R143, R180, R203, and R207) are distributed along a boundary between the hydrophobic and hydrophilic regions of the dimer surface (Fig. 1*C* and *SI Appendix*, Fig. S4). They are conserved across all amino acid sequences of the membrane-bound AOXs shown in *SI Appendix*, Fig. S5, and their locations make these residues ideal candidates to interact with the negatively charged phospholipids head groups of membranes.

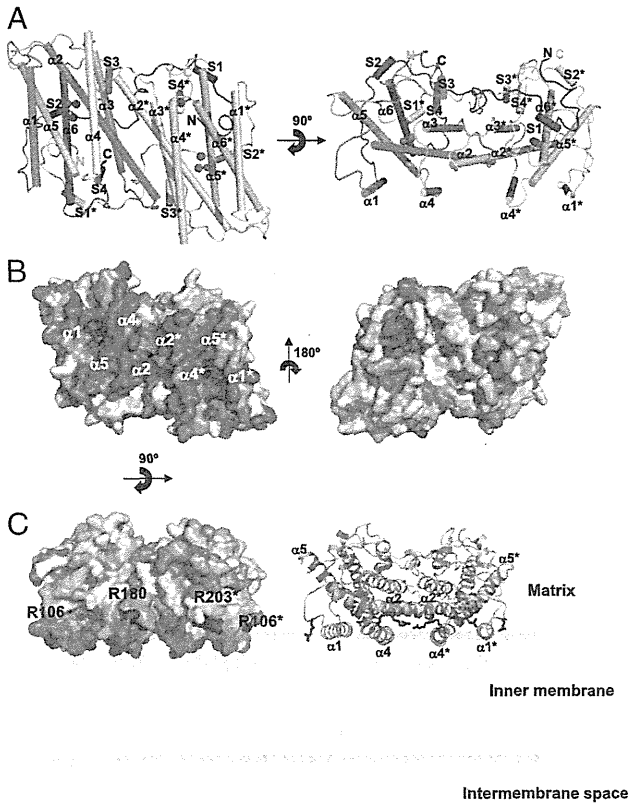

Fig. 1. Structure of TAO. Long helices are labeled α1 to α6 and short ones S1 to S4. Diiron and hydroxo atoms are shown as magenta spheres. (*A*) Dimeric structure of TAO viewed roughly perpendicular (*Left*) and parallel (*Right*) to the helix axes. Helices are shown as cylinders. Chain A is colored in rainbow from blue (N terminus) to red (C terminus) and chain B in pink. (*B*) Surface representation of the TAO dimer showing the hydrophobic (*Left*) and hydrophilic (*Right*) surfaces. Colors are according to the following hydrophobicity scale: red, high hydrophobicity; white, low hydrophobicity (www.pymolwiki.org/index.php/Color_h). (*C*) Proposed binding model of the TAO dimer to membranes shown by surface (*Left*) and cartoon (*Right*) representations. The hydrophobic region on the molecular surface of the TAO dimer faces the membrane. Conserved basic amino acid residues, which are distributed along a boundary between the hydrophobic and hydrophilic regions of the dimer surface, are colored in blue. Residue names are labeled in black (asterisk denotes in chain B).

Structure of Diiron Active Site. The structure of the diiron active site was refined as an oxidized Fe(III)-Fe(III) form with a single hydroxo-bridge (Fig. 2 and *SI Appendix*, Fig. S6), as previously predicted from spectroscopic studies (19, 20). The active site, which is located in a hydrophobic environment deep inside the TAO molecule, is composed of the diiron center and four glutamate (E123, E162, E213, and E266) and two histidine residues (H165 and H269), all of which are completely conserved (*SI Appendix*, Fig. S5). In addition, the conserved hydrophobic residues (L122, A126, L212, A216, Y220, and I262) are within 6 Å of the diiron center (Fig. 2*A*). The average Fe1–Fe2 distance of the four monomers in the asymmetric unit is 3.3 ± 0.2 Å and, in addition to the hydroxo-bridge, Fe1 and Fe2 are bridged by E162 and E266 and furthermore coordinated in a bidentate fashion by E123 and E213, respectively, thereby resulting in a five-coordinated diiron center possessing a distorted square pyramidal geometry (Fig. 2*B* and *SI Appendix*, Fig. S6 and Table S2). The most striking feature of the diiron active site in the oxidized state is that, as predicted from our earlier FTIR studies (26), histidine residues (H165 and H269) are too distant from both Fe1 and Fe2 (H165: 3.3~4.0 Å, H269: 3.8~4.4 Å) to coordinate to the diiron center. They do, however, form hydrogen bonds with E123, N161, E162, E213, and D265. N161 and D265 are situated in the center of the hydrogen-bond network and extend the network to W65, Y246, and W247. These residues, apart from W65, are again completely conserved (*SI Appendix*, Fig. S5), suggesting that the hydrogen bond network is important for the stabilization of the AOX active site. To our knowledge, TAO is the only structure of

BIOCHEMISTRY

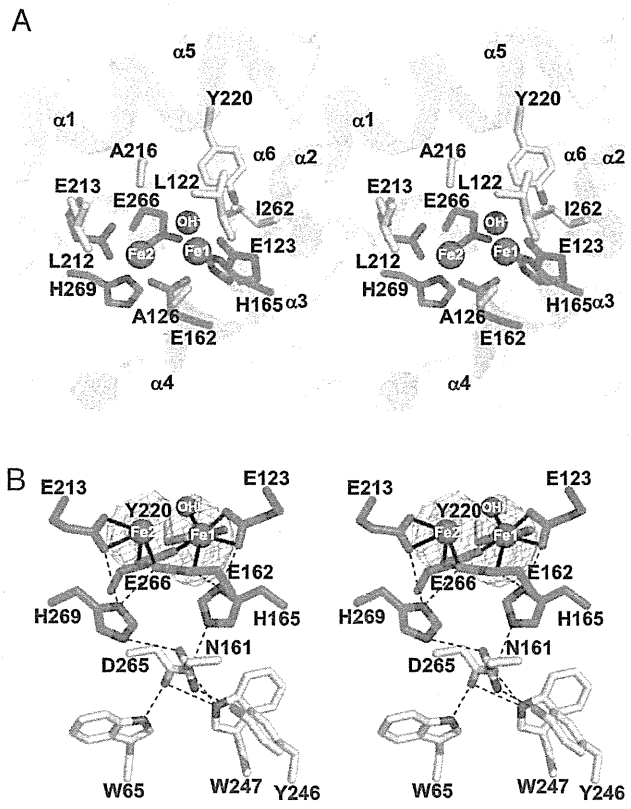

Fig. 2. Diiron structure of TAO. (*A*) Stereo view of the diiron active site and its environment. Diiron and hydroxo atoms are shown as magenta spheres, four glutamate and two histidine residues important for diiron binding as green sticks, neighboring residues within 6 Å of the diiron in yellow, nitrogen in blue, and oxygen in red. (*B*) Stereo view of the coordinate bonds (solid lines) and hydrogen bonds (dashed lines) of the diiron active site. Sigma-A weighted electron density map calculated from the refined model of the ligand-free TAO with the diiron centers omitted from the phase calculation is also shown. Contour levels are 1.0 σ (blue) and 3.0 σ (orange). H165 forms hydrogen bonds with E123, E162, and N161 and H269 with E162, E213, and N161. N161, which is situated in the center of the hydrogen network, forms additional hydrogen bonds with Y246 and D265. D265 forms hydrogen bonds with W65 and W247.

an oxidized diiron active site that is ligated solely by carboxylate ligands. In contrast, diiron active sites of soluble diiron proteins with known structures, Δ^4 ACP desaturase (27) (PDB ID code 2UW1), methane monooxygenase (28) (PDB ID code 1MMO), rubrerythrin (29) (PDB ID code 1LKM), and ribonucleotide reductase R2 subunit (30) (PDB ID code 1RIB), are all coordinated by at least one if not two histidine residues.

Important Tyrosine Residues. Similar to ribonucleotide reductase, tyrosine residues have also been proposed to play an essential role in the catalytic cycle of AOX (1, 31, 32). Scrutiny of *SI Appendix*, Fig. S5 reveals that although there seem to be four conserved tyrosine residues (Y198, Y211, Y220, and Y246), only three of which (not Y211) are totally conserved across all amino acid sequences of membrane-bound AOXs, including the plastid AOX (33). Y220 is buried deep within the four-helix bundle and within 4 Å of the diiron center (Fig. 2*A*), making it the most likely candidate for the amino acid radical involved in the catalytic cycle (32). Indeed, Y220 is absolutely conserved across all AOXs sequenced to date, and mutational analyses have unequivocally demonstrated that this residue is critical for enzymatic activity of all AOXs (1, 33). Y198 has been proposed to be involved in ubiquinol binding, although its mutation does not lead to the complete loss of activity (18, 34). The crystal structure of TAO (*SI Appendix*, Fig. S7) indicates that Y198, located on the C-terminal portion of helix α4, is separated by more than 15 Å from the diiron center and forms a hydrogen bond with a conserved H206 protruding from the N-terminal portion of helix α5. Such a position suggests it probably stabilizes the structure of TAO rather than being directly involved in ubiquinol binding. Although Y246 on helix S3 is located 10.7 ± 0.2 Å from the diiron center, which is within electron tunneling distance [<14 Å (35)], it is more likely to be involved in the hydrogen-bonding network rather than electron transport, because it is 2.9 ± 0.2 Å from N161 in helix α3 (Fig. 2*B* and *SI Appendix*, Fig. S7). This notion is supported by the result that a Y246A mutant retains some activity (1, 34), which would not be the case if it were essential for electron transfer.

Binding Mode of the Potent Inhibitor AF2779OH. Until recently little structural information was available on the mode of AF binding to TAO, even given its specificity. Inhibitor kinetic studies indicated that AF showed a mixed-type inhibition against ubiquinol (23), suggesting that the ring moiety and the geranyl portions of AF are important for the interaction of the inhibitor with TAO. To investigate whether this was the case, an AF derivative lacking the furanone ring was synthesized (AF2779OH: 5-chloro-3-[(2*E*,6*E*)-8-hydroxy-3,7-dimethylnona-2,6-dienyl]-2,4-dihydroxy-6-methylbenzaldehyde; Fig. 3*A*). AF2779OH possesses similar inhibitory properties (IC_{50} = 0.48 nM for TAO; minimum inhibitory concentration = 30 nM for *T. brucei brucei*) to AF, indicating that the furanone ring is indeed not critical for inhibitory activity, thereby rendering it useful to determine the location of AF binding to TAO. A crystal of the TAO–AF2779OH complex was prepared by soaking in the cryoprotectant solution supplemented with the inhibitor and the structure determined at 2.6 Å by molecular replacement using the inhibitor-free TAO structure as a template (*SI Appendix*, Table S1 and Fig. S1*B*). In addition, the crystal structure of TAO complexed with CCB, another AF derivative (5-chloro-3-[(2E)-3,7-dimethylocta-2,6-dienyl]-2,4-dihydroxy-6-methylbenzaldehyde), was also determined at 2.3 Å resolution (*SI Appendix*, Table S1 and Fig. S1*C*). *SI Appendix*, Figs. S8 and S9 show that CCB is bound to the enzyme in a manner similar to AF2779OH. CCB also strongly inhibits TAO (IC_{50} = 0.20 nM for TAO); however, unlike AF and AF2779OH, it is toxic to mice. Given the toxicity of CCB we will therefore focus further discussion on the structure of TAO complexed with AF2779OH, because it is a safer drug candidate for trypanosomiasis.

Fig. 3 *B* and *C* show the dimeric structure of the TAO–AF2779OH complex and residues around the bound AF2779OH, respectively. The binding cavity of AF2779OH is located near the membrane surface between helices α1 and α4 and is lined by 16 highly conserved residues (V92, R96, F99, R118, C119, F121, L122, E123, V125, M190, L212, E213, E215, A216, T219, and Y220) plus C95 (Fig. 3*C* and *SI Appendix*, Figs. S5 and S8 and Table S3). It is also apparent from Fig. 3*C* and *SI Appendix*, Fig. S8 and Table S3 that the aromatic head of AF2779OH is located close to the diiron active site and the C2–OH forms hydrogen bonds with R118 and T219. In addition, the aldehyde oxygen at the C1 position interacts with E123 through a hydrogen bond network, C1–CH = O···C119–SH···Y220–OH···E123–COO^-, in the B and D subunit, whereas the aldehyde oxygens of the A and C subunits form an intrasubunit hydrogen bond with C2–OH. These hydrogen bonds are also observed in the TAO–CCB complex and seem to be important for the potent inhibitory activities of both inhibitors. Indeed, IC_{50} values of AF derivatives lacking this aldehyde group (K2-9 and K4-9 in *SI Appendix*, Fig. S10) increase substantially (36). It is also likely that van der Waals contacts formed between AF2779OH and TAO (*SI Appendix*, Table S3) contribute to the potent effect of these inhibitors (36). In the inhibited enzymes the distances between H165 and Fe1 (2.3 ± 0.1 and 2.4 ± 0.1 Å for AF2779OH and CCB, respectively) are shorter than that observed in the inhibitor-free structure (3.5 ± 0.3 Å), and hence H165 can now

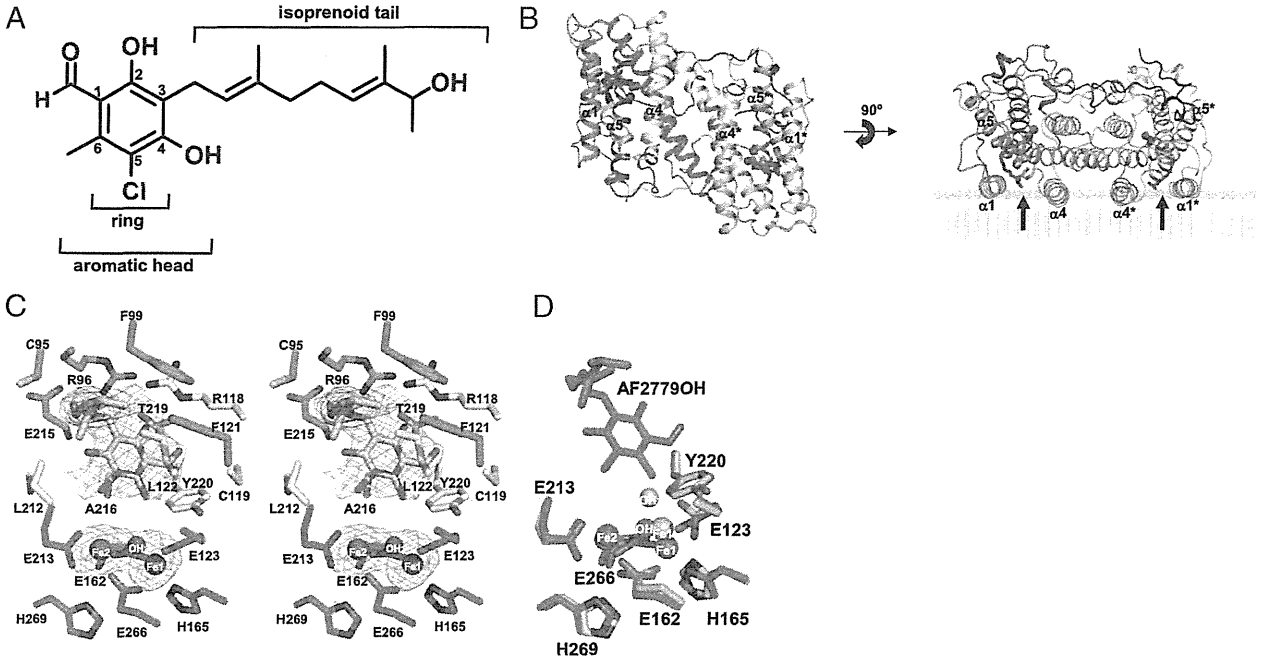

Fig. 3. Structure of the TAO–AF2779OH complex. (*A*) The chemical structure of AF2779OH. (*B*) Overall structure of the TAO–AF2779OH complex. AF2779OH is shown as a red stick. Chains A and B are shown as rainbow (colored blue to red from N to C terminus) and gray, respectively. The AF2779OH-binding cavity is shown by an arrow. (*C*) Stereo view of the AF2779OH binding region of chain A. The residues that interact with AF2779OH (pink stick) -ring and -tail are shown as yellow and cyan sticks, respectively. N, O, and Cl atoms are colored in blue, red, and green, respectively. Sigma-A weighted electron density map calculated from the refined model of the TAO–AF2779OH complex with the diiron centers and AF2779OH molecules omitted from the phase calculation is also shown. Contour levels are 1.0 σ (blue) and 3.0 σ (orange). (*D*) Superimposed diiron active sites of AF2779OH-free (light pink) and -bound (green) forms of TAO. The binding of AF2779OH causes the formation of a coordinate bond between H165 and Fe1.

coordinate with Fe1, unlike H269, which is still separated by 4.3 ± 0.2 Å from Fe2 in both cases (Fig. 3*D* and *SI Appendix*, Fig. S12 and Table S2).

Mutational Analysis of Functionally Relevant Residues. *SI Appendix*, Table S4 summarizes the catalytic activities of the mutated recombinant proteins that were measured in isolated membrane fractions from each *Escherichia coli* culture. It is apparent from *SI Appendix*, Table S4 that all mutated residues that interact either with the diiron (E213A) or the inhibitor (R118A, R118Q, L122A, L122N, E215A, A216L, A216N, T219V, and Y220F; Fig. 4) resulted in almost complete loss of ubiquinol oxidizing activity. Furthermore, the Y246A mutant, which participates in the hydrogen bond network (Fig. 2), also resulted in significant inhibition of catalytic activity. We believe that these residues are important for the correct conformation of the diiron center and interaction with AF2779OH and are consistent with the crystal structure.

Ubiquinol Binding Model. In addition to the inhibitor-binding cavity observed in Figs. 3*B* and 5 *A* and *C*, which is comparable to that observed in other monotopic proteins such as prostaglandin H_2 synthase (37), CAVER protein-analysis software (38) predicts that there is another possible hydrophobic cavity near the membrane surface (Fig. 5 *A* and *D*). This second cavity connects the diiron active site with the membrane exterior and interacts with the inhibitor-binding cavity at the active site. It is formed by residues from helices α1 (R96 and D100), α2 (R118, L122, E123, and A126), α3 (E162 and H165), α5 (L212, E213, E215, A216, and T219), and α6 (E266), which, similar to that observed in the inhibitor-binding cavity, are also highly conserved (*SI Appendix*, Fig. S5). It is apparent from Fig. 5 *A* and *D* that a part of the aromatic head group of AF2779OH enters this second cavity. Based on the structure of the TAO–AF2779OH complex, a ubiquinol-binding model was built by superposing a ubiquinol molecule onto the bound AF2779OH. The model (Fig. 5*B*) indicates that the distance between ubiquinol C4–OH and Fe2 is 4.3 Å and C1–OH is connected to the outside of TAO through a hydrogen bond network, C1–OH···R118···D100 (Fig. 5*B*). On the basis of the structures reported in this study we propose that each hydrophobic cavity binds one ubiquinol close to the active site with their quinol rings located at the bottom of each cavity in a manner similar to AF2779OH. Although the exact route of electron transfer for the four-electron reduction of oxygen to water in any alternative oxidase is unresolved at the present time, we suggest the process involves both ubiquinols and Tyr220

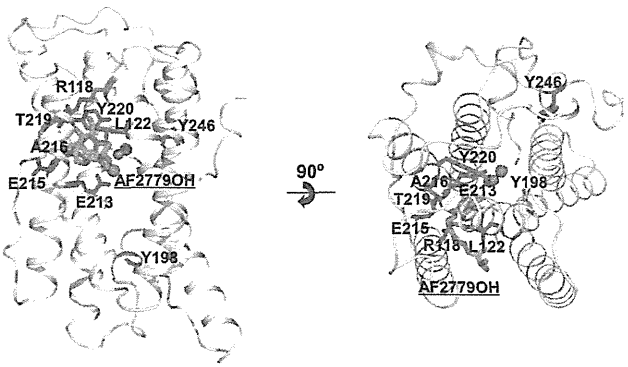

Fig. 4. Location of the recombinant TAO mutations within the protein. Diiron and hydroxo atoms are shown as magenta spheres. AF2779OH is shown as a cyan stick. Red sticks show the mutated residues that almost completely abolished activity (specific activity <10%), whereas yellow sticks show the mutated residues that retained some residual activity (specific activity ≥10%).

(39). During the sequential electron reduction process we suggest that following the activation of oxygen, free radicals are generated on a tightly bound ubiquinol and Tyr220. The ubisemiquinol is then reoxidized by the tyrosine radical generated during the catalytic cycle and the reduction process is completed following full oxidation of a loosely bound ubiquinol (39).

Conclusions

The TAO structures reported in this study are a high-resolution view of a membrane bound diiron-carboxylate protein. Although the crystal structures support earlier modeling studies (13, 14, 22) that suggested that the alternative oxidases are monotopic proteins in which the diiron active site is coordinated by carboxylate and histidine residues, they did reveal that in the oxidized state only carboxylate residues act as the coordinating ligands. Such a primary ligation sphere, although unusual for diiron proteins in the oxidized state, is, however, consistent with our earlier reduced minus oxidized IR difference spectra (26). This study clearly demonstrated that upon reduction of purified TAO there was a net protonation of at least one carboxylate residue in addition to alterations in the signals associated with histidine residues consistent with the notion that the oxidation–reduction cycle of the alternative oxidases involves major conformational perturbations and carboxylate shifts. The structure has also revealed that the redox-active Y220, which is totally conserved across all AOXs (1), is within 4 Å of the active site. Such a close-range electron transfer position, comparable to that observed in the R2 subunit of ribonucleotide reductase (31), is further support for the suggestion that radicals play a key role in the AOX catalytic cycle (39).

In addition to providing a structural insight into the active site of this enigmatic protein our structures have also revealed the nature of the inhibitor binding site. The binding site of our AF derivative was within 4 Å of not only the diiron center but also Y220 and resulted in some dramatic conformational changes such that H165 moved within ligating distance of Fe (1). CAVER protein analysis software (38) suggested that the inhibitor-binding cavity connects at the diiron center with an additional cavity, which could also serve as a ubiquinone binding site.

In conclusion, we believe that the structures presented in this report will contribute to a more complete understanding of the function and inhibition of all AOXs. It will not only be beneficial for the control of trypanosomiasis and other human diseases, such as cryptosporidiosis and candidiasis, but also for the control of plant diseases caused by phytopathogenic fungi (1, 40).

Materials and Methods

Crystallization. The oxidized form of alternative oxidase from *Trypanosoma brucei brucei* was expressed, purified, and crystallized essentially according to the method described previously (23, 24) using 28–34% (wt/vol) PEG 400, 100 mM imidazole buffer (pH 7.4), and 500 mM potassium formate as the reservoir solution. Detailed information is presented in *SI Appendix, SI Materials and Methods*.

Data Collection and Phasing. For phasing by the single-wavelength anomalous dispersion (SAD) method, anomalous scattering effects caused by Fe were measured to 3.2 Å resolution. The dataset was processed and scaled with HKL2000 (41). The program SOLVE (42) was used to locate and refine four "diiron sites" (figure of merit = 0.195). The RESOLVE (43) program was used for solvent flattening (figure of merit = 0.645). The resulting electron density map was clear enough to trace the TAO molecules. Initial models were built

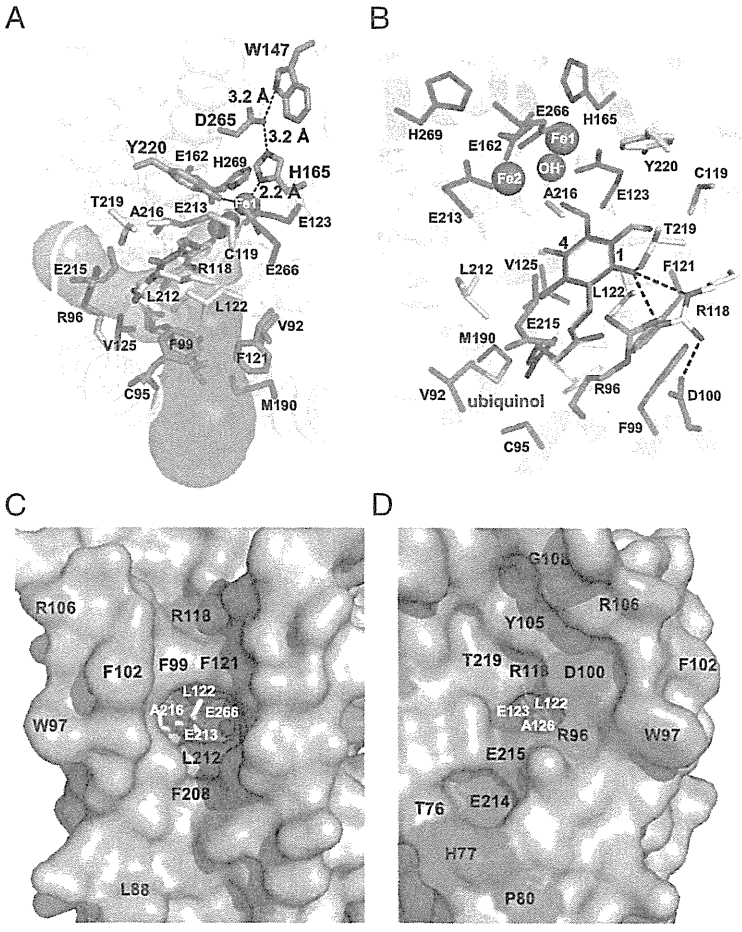

Fig. 5. Putative ubiquinol binding cavities in TAO. (*A*) Two hydrophobic cavities predicted by CAVER protein-analysis software (38). The bound AF2779OH (isoprenoid tail) occupies the green cavity. Putative residues involved in electron transfer are shown as orange sticks. (*B*) Ubiquinol binding model predicted by the superposition of a ubiquinol molecule (purple stick) onto the bound AF2779OH (translucent white stick) of the TAO–AF2779OH complex. Magenta spheres are diiron (Fe–OH^-–Fe), the green stick represents residues coordinating to diiron, and yellow and cyan sticks are residues interacting with the aromatic head and isoprenoid tail, respectively. Hydrogen bonds are depicted as dotted lines. Surface views of the (*C*) green and (*D*) orange cavities shown in *A*. Cyan and pink colors stand for conservation of AOX residues in all eight and over four organisms in *SI Appendix*, Fig S5, respectively.

using RESOLVE (43) and BUCANER (43). Detailed analysis of diffraction data showed that the crystal used for the data collection of Fe-SAD was pseudohemihedral twinning. Amplitude-based twin-refinement using REFMAC5 (45) decreased R_{work}/R_{free} drastically from 0.307/0.363 to 0.250/0.310. X-ray diffraction data of ligand-free TAO and AF derivatives complex crystals were collected to 2.85, 2.6, and 2.3 Å resolution, respectively. All datasets were processed and scaled with HKL2000 (42). Detail information is presented in *SI Appendix, SI Materials and Methods*.

Refinement. The initial model of inhibitor-free TAO was determined by molecular replacement (MR) using the model obtained by SAD (3.2 Å resolution) as a search model. The program Phaser (46) in CCP4i was used for MR. The models of ligand-free TAO and TAO-AF2779OH complex were rebuilt with reference to the well-refined model of the TAO–CCB complex at 2.3 Å resolution. Manual rebuilding and crystallographic refinement of all structures were performed using COOT (47) and REFMAC5 (45). All structures were refined by amplitude-based twin-refinement in REFMAC5 (45) to final R_{work}/R_{free} values of 0.192/0.247 (twin fraction of 0.476), 0.214/0.256 (twin fraction of 0.552), and 0.185/0.227 (twin fraction of 0.527) for ligand-free TAO, TAO–AF2779OH, and TAO–CCB, respectively. The omit electron density maps of ligand-free TAO, TAO–AF2779OH, and TAO–CCB around helix 5 are shown in *SI Appendix*, Fig. S14. On average, about 30 residues of N and C termini of TAO were missing as a result of flexibility. Data collection and structural refinement statistics are summarized in *SI Appendix*, Table S1. Figures showing protein structures were prepared with the graphics program PyMol (www.pymol.org). Detailed information is presented in *SI Appendix, SI Materials and Methods*.

ACKNOWLEDGMENTS. We thank all staff members of beamlines BL44XU and BL41XU at SPring-8, BL17A at the High Energy Accelerator Research Organization Photon Factory for their help with X-ray diffraction data collection. This work was supported in part by Grant-in-Aid for Young Scientists (B) 21790402 (to Y.K.); Grant-in-Aid for Scientific Research (C) 23570131 (to T.S.); Creative Scientific Research Grant 18GS0314 (to K.K.); Grant-in-Aid for Scientific Research on Priority Areas 18073004 (to K.K.) from the Japanese Society for the Promotion of Science and by a grant from the Targeted Proteins Research Program (to T.N., T.A., T.H., A.T., M.I., S.M., S.H., and K.K.) from the Japanese Ministry of Education, Science, Culture, Sports and Technology; a grant-in-aid for research on emerging and reemerging infectious diseases from the Japanese Ministry of Health and Welfare (to K.K.); and by the Programme for Promotion of Basic and Applied Researches for Innovations in Bio-Oriented Industry (S.H. and K.K.). A.L.M. gratefully acknowledges the Biotechnology and Biological Sciences Research Council for financial support. A.L.M. and K.K. acknowledge support from the Prime Minister's Initiative for International Education fund for collaborative twinning.

1. Moore AL, Albury MS (2008) Further insights into the structure of the alternative oxidase: From plants to parasites. *Biochem Soc Trans* 36(Pt 5):1022–1026.
2. McDonald AE, Vanlerberghe GC (2006) Origins, evolutionary history, and taxonomic distribution of alternative oxidase and plastoquinol terminal oxidase. *Comp Biochem Physiol Part D Genomics Proteomics* 1(3):357–364.
3. Chaudhuri M, Ajayi W, Hill GC (1998) Biochemical and molecular properties of the *Trypanosoma brucei* alternative oxidase. *Mol Biochem Parasitol* 95(1):53–68.
4. Roberts CW, et al. (2004) Evidence for mitochondrial-derived alternative oxidase in the apicomplexan parasite *Cryptosporidium parvum*: A potential anti-microbial agent target. *Int J Parasitol* 34(3):297–308.
5. Chaudhuri M, Ott RD, Hill GC (2006) Trypanosome alternative oxidase: From molecule to function. *Trends Parasitol* 22(10):484–491.
6. Phillips MA (2012) Stoking the drug target pipeline for human African trypanosomiasis. *Mol Microbiol* 86(1):10–14.
7. Zíkova A, Schnaufer A, Dalley RA, Panigrahi AK, Stuart KD (2009) The Fo-F1-ATP synthase complex contains novel subunits and is essential for procyclic *Trypanosoma brucei*. *PLoS Pathog* 5:1–15.
8. Opperdoes FR, Borst P, Bakker S, Leene W (1977) Localization of glycerol-3-phosphate oxidase in the mitochondrion and particulate NAD+-linked glycerol-3-phosphate dehydrogenase in the microbodies of the bloodstream form to *Trypanosoma brucei*. *Eur J Biochem* 76(1):29–39.
9. Nihei C, Fukai Y, Kita K (2002) Trypanosome alternative oxidase as a target of chemotherapy. *Biochim Biophys Acta* 1587(2–3):234–239.
10. Minagawa N, et al. (1997) An antibiotic, ascofuranone, specifically inhibits respiration and in vitro growth of long slender bloodstream forms of *Trypanosoma brucei brucei*. *Mol Biochem Parasitol* 84(2):271–280.
11. Yabu Y, et al. (2003) The efficacy of ascofuranone in a consecutive treatment on *Trypanosoma brucei brucei* in mice. *Parasitol Int* 52(2):155–164.
12. Yabu Y, et al. (2006) Chemotherapeutic efficacy of ascofuranone in *Trypanosoma vivax*-infected mice without glycerol. *Parasitol Int* 55(1):39–43.
13. Andersson ME, Nordlund P (1999) A revised model of the active site of alternative oxidase. *FEBS Lett* 449(1):17–22.
14. Berthold DA, Andersson ME, Nordlund P (2000) New insight into the structure and function of the alternative oxidase. *Biochim Biophys Acta* 1460(2-3):241–254.
15. Albury MS, Affourtit C, Moore AL (1998) A highly conserved glutamate residue (Glu-270) is essential for plant alternative oxidase activity. *J Biol Chem* 273(46): 30301–30305.
16. Ajayi WU, Chaudhuri M, Hill GC (2002) Site-directed mutagenesis reveals the essentiality of the conserved residues in the putative diiron active site of the trypanosome alternative oxidase. *J Biol Chem* 277(10):8187–8193.
17. Albury MS, Affourtit C, Crichton PG, Moore AL (2002) Structure of the plant alternative oxidase. Site-directed mutagenesis provides new information on the active site and membrane topology. *J Biol Chem* 277(2):1190–1194.
18. Nakamura K, et al. (2005) Mutational analysis of the *Trypanosoma vivax* alternative oxidase: The $E(X)_6Y$ motif is conserved in both mitochondrial alternative oxidase and plastid terminal oxidase and is indispensable for enzyme activity. *Biochem Biophys Res Commun* 334(2):593–600.
19. Berthold DA, Voevodskaya N, Stenmark P, Gräslund A, Nordlund P (2002) EPR studies of the mitochondrial alternative oxidase. Evidence for a diiron carboxylate center. *J Biol Chem* 277(46):43608–43614.
20. Moore AL, et al. (2008) Compelling EPR evidence that the alternative oxidase is a diiron carboxylate protein. *Biochim Biophys Acta* 1777(4):327–330.
21. Nordlund P, Eklund H (1995) Di-iron-carboxylate proteins. *Curr Opin Struct Biol* 5(6): 758–766.
22. Berthold DA, Stenmark P (2003) Membrane-bound diiron carboxylate proteins. *Annu Rev Plant Biol* 54:497–517.
23. Kido Y, et al. (2010) Purification and kinetic characterization of recombinant alternative oxidase from *Trypanosoma brucei brucei*. *Biochim Biophys Acta* 1797(4): 443–450.
24. Kido Y, et al. (2010) Crystallization and preliminary crystallographic analysis of cyanide-insensitive alternative oxidase from *Trypanosoma brucei brucei*. *Acta Crystallogr Sect F Struct Biol Cryst Commun* 66(Pt 3):275–278.
25. Lomize MA, Pogozheva ID, Joo H, Mosberg HI, Lomize AL (2012) OPM database and PPM web server: Resources for positioning of proteins in membranes. *Nucleic Acids Res* 40(Database issue):D370–D376.
26. Maréchal A, Kido Y, Kita K, Moore AL, Rich PR (2009) Three redox states of *Trypanosoma brucei* alternative oxidase identified by infrared spectroscopy and electrochemistry. *J Biol Chem* 284(46):31827–31833.
27. Guy JE, Whittle E, Kumaran D, Lindqvist Y, Shanklin J (2007) The crystal structure of the ivy Δ^4-16:0-ACP desaturase reveals structural details of the oxidized active site and potential determinants of regioselectivity. *J Biol Chem* 282(27):19863–19871.
28. Rosenzweig AC, Frederick CA, Lippard SJ, Nordlund P (1993) Crystal structure of a bacterial non-haem iron hydroxylase that catalyses the biological oxidation of methane. *Nature* 366(6455):537–543.
29. Jin S, Kurtz DM, Jr., Liu ZJ, Rose J, Wang BC (2002) X-ray crystal structures of reduced rubrerythrin and its azide adduct: A structure-based mechanism for a non-heme diiron peroxidase. *J Am Chem Soc* 124(33):9845–9855.
30. Nordlund P, Eklund H (1993) Structure and function of the *Escherichia coli* ribonucleotide reductase protein R2. *J Mol Biol* 232(1):123–164.
31. Schmidt PP, Rova U, Katterle B, Thelander L, Gräslund A (1998) Kinetic evidence that a radical transfer pathway in protein R2 of mouse ribonucleotide reductase is involved in generation of the tyrosyl free radical. *J Biol Chem* 273(34):21463–21472.
32. Affourtit C, Albury MS, Crichton PG, Moore AL (2002) Exploring the molecular nature of alternative oxidase regulation and catalysis. *FEBS Lett* 510(3):121–126.
33. McDonald AE (2009) Alternative oxidase: What information can protein sequence comparisons give us? *Physiol Plant* 137(4):328–341.
34. Albury MS, Elliott C, Moore AL (2010) Ubiquinol-binding site in the alternative oxidase: Mutagenesis reveals features important for substrate binding and inhibition. *Biochim Biophys Acta* 1797(12):1933–1939.
35. Page CC, Moser CC, Chen X, Dutton PL (1999) Natural engineering principles of electron tunnelling in biological oxidation-reduction. *Nature* 402(6757):47–52.
36. Saimoto H, Kido Y, Haga Y, Sakamoto K, Kita K (2013) Pharmacophore identification of ascofuranone, potent inhibitor of cyanide-insensitive alternative oxidase of Trypanosoma brucei. *J Biochem* 153(3):267–273.
37. Picot D, Loll PJ, Garavito RM (1994) The X-ray crystal structure of the membrane protein prostaglandin H_2 synthase-1. *Nature* 367(6460):243–249.
38. Medek P, Benes P, Sochor J (2007) Computation of tunnels in protein molecules using Delaunay triangulation. *J WSCG* 15:107–114.
39. Moore AL, et al. (2013) Unraveling the heater – New insights into the structure of the alternative. *Annu Rev Plant Biol*, in press.
40. Fernández-Ortuño D, Torés JA, de Vicente A, Pérez-García A (2008) Mechanisms of resistance to QoI fungicides in phytopathogenic fungi. *Int Microbiol* 11(1):1–9.
41. Otwinowski Z, Minor W (1997) Processing of X-ray diffraction data collected in oscillation mode. *Methods Enzymol* 276:307–326.
42. Terwilliger TC, Berendzen J (1999) Automated MAD and MIR structure solution. *Acta Crystallogr D Biol Crystallogr* 55(Pt 4):849–861.
43. Terwilliger TC (2000) Maximum-likelihood density modification. *Acta Crystallogr D Biol Crystallogr* 56(Pt 8):965–972.
44. Cowtan K (2006) The Buccaneer software for automated model building. 1. Tracing protein chains. *Acta Crystallogr D Biol Crystallogr* 62(Pt 9):1002–1011.
45. Murshudov GN, Vagin AA, Dodson EJ (1997) Refinement of macromolecular structures by the maximum-likelihood method. *Acta Crystallogr D Biol Crystallogr* 53(Pt 3):240–255.
46. McCoy AJ, Grosse-Kunstleve RW, Storoni LC, Read RJ (2005) Likelihood-enhanced fast translation functions. *Acta Crystallogr D Biol Crystallogr* 61(Pt 4):458–464.
47. Emsley P, Cowtan K (2004) Coot: model-building tools for molecular graphics. *Acta Crystallogr D Biol Crystallogr* 60(Pt 12 Pt 1):2126–2132.

J. Biochem. 2013;154(1):77–84 doi:10.1093/jb/mvt037

JB THE JOURNAL OF BIOCHEMISTRY

Biochemical characterization of highly active *Trypanosoma brucei gambiense* glycerol kinase, a promising drug target

Received March 6, 2013; accepted March 31, 2013; published online April 25, 2013

Emmanuel Oluwadare Balogun[1,2,3], Daniel Ken Inaoka[1], Tomoo Shiba[2], Yasutoshi Kido[1], Takeshi Nara[4], Takashi Aoki[4], Teruki Honma[5], Akiko Tanaka[5], Masayuki Inoue[6], Shigeru Matsuoka[6], Paul AM. Michels[7], Shigeharu Harada[2,*] and Kiyoshi Kita[1,†]

[1]Department of Biomedical Chemistry, Graduate School of Medicine, The University of Tokyo, 7-3-1 Hongo, Bunkyo-ku, Tokyo 113-0033, Japan; [2]Department of Applied Biology, Graduate School of Science and Technology, Kyoto Institute of Technology, Sakyo-ku, Kyoto 606-8585, Japan; [3]Department of Biochemistry, Ahmadu Bello University, Zaria 2222, Nigeria; [4]Department of Molecular and Cellular Parasitology, Juntendo University School of Medicine, Tokyo 113-8421, Japan; [5]Systems and Structural Biology Center, RIKEN, Tsurumi, Yokohama 230-0045, Japan; [6]Graduate School of Pharmaceutical Sciences, The University of Tokyo, Tokyo 113-0033, Japan; and [7]Research Unit for Tropical Diseases, de Duve Institute and Laboratory of Biochemistry, Université catholique de Louvain, Avenue Hippocrate 74, B-1200 Brussels, Belgium

*Shigeharu Harada, Department of Applied Biology, Graduate School of Science and Technology, Kyoto Institute of Technology, Sakyo-ku, Kyoto 606-8585, Japan. Tel: +81-7-5724-7541, Fax: +81-7-5724-7541, email: harada@kit.ac.jp

†Kiyoshi Kita, Department of Biomedical Chemistry, Graduate School of Medicine, University of Tokyo, 7-3-1 Hongo, Bunkyo-ku, Tokyo 113-0033, Japan. Tel: +81-3-5841-3526, Fax: +81-3-5841-3444, email: kitak@m.u-tokyo.ac.jp

Human African trypanosomes are blood parasites that cause sleeping sickness, a debilitating disease in sub-Saharan Africa. Glycerol kinase (GK) of these parasites additionally possesses a novel property of reverse catalysis. GK is essential to blood stream form trypanosome, and therefore a promising drug target. Here, utilizing recombinant DNA technology an optimized procedure for obtaining large amount of the purified protein was established. Furthermore, biochemical data on its enzymology are reported. The protein was maximally active at pH 6.8 over a temperature range of 25–70°C, with activation energy of 34.02 ± 0.31 kJ mol^{-1}. The enzyme catalyses a reversible bisubstrate [ADP and glycerol 3-phosphate (G3P)]-biproduct (ATP and glycerol) reaction. It has K_m of 0.90 and 5.54 mM for ADP and G3P, respectively, and V_{max} of 25.3 and 20.0 μmol min^{-1} mg^{-1}, respectively. Unexpectedly, the enzyme lost more than 50% of its activity in 48 h at 4°C in 0.1 M sodium phosphate buffer pH 6.8 containing 10 mM $MgSO_4$. However, perfect stabilization of the GK for more than 4 weeks was achieved in the presence of its natural ligands and cofactor. Using this stabilized protein, crystals of trypanosome GK with better resolution were obtained. This will accelerate the success of GK inhibitor development for drug design.

Keywords: African trypanosomes/characterization/crystallization/drug design/glycerol kinase.

Abbreviations: E_a, activation energy; GK, glycerol kinase; G3P, glycerol 3-phosphate; IPTG, isopropyl β-D-thiogalactopyranoside; LB, Luria-Bertani; OD_{600}, optical density at 600 nm; PMSF, phenylmethylsolfonyl fluoride; Tbg, *Trypanosoma brucei gambiense*; Tbr, *Trypanosoma brucei rhodesiense*.

The African human trypanosomes are *Trypanosoma brucei gambiense* (Tbg) and *Trypanosoma brucei rhodesiense* (Tbr), which cause the disease known as sleeping sickness. They are transmitted through the bites of blood sucking insect called tsetse fly (*1*). Once in the human host, they multiply rapidly in the bloodstream, invade the central nervous system and eventually lead to death if untreated (*2*). As a result of problems, such as toxicity and resistance, the present chemotherapeutic options are still far from ideal (*3*, *4*). Therefore, these necessitate the need to develop safer and more effective drugs having well-defined mechanism(s) of action. To achieve this, highly selective compounds that affect novel and validated essential molecular targets in the parasites must be developed. The energy metabolism pathway of these parasites has been recognized as such a novel drug target (*5*, *6*). African trypanosomes bloodstream forms (BSFs) derive all their energy needs from the glycosome-compartmentalized glycolytic pathway, generating a net of two ATP molecules from the catabolism of each molecule of glucose under aerobic condition (*7–9*). This optimum ATP production is tightly coupled to the activity of mitochondrially localized trypanosome alternative oxidase (TAO) (*10*, *11*). The summation of this vital role of TAO and its absence in mammals portrays it as a good target of chemotherapy. Our group found ascofuranone (AF) and some of its derivatives to be specific sub-nanomolar inhibitor of TAO (*12*). However, *in vitro* and *in vivo* studies have shown that glycerol kinase (GK) rescue the BSFs from AF-induced killing (*10*, *11*).

GK of BSFs is necessary for their survival when TAO is inhibited; in addition to the widely known GK-catalysed reaction—transphosphorylation of glycerol from ATP (forward reaction), the trypanosome GK is able to catalyse the thermodynamically unfavourable reaction of phosphoryl transfer from glycerol 3-phosphate (G3P) to ADP, forming ATP and glycerol

(reverse reaction). This unique reverse reaction is particularly important to these protozoan parasites when the mitochondrial function is impaired during anaerobiosis or by the presence of TAO inhibitors. Under such condition, the parasites resort to anaerobic glycolysis during which the GK provide them with the only ATP for survival (*6*, *13*). This reverse catalysis of trypanosome GK, in addition to its lack of enzymatic regulation, distinguishes it from the GK of their hosts (*14*, *15*). Although the parasite GK is a drug target candidate, to date, all efforts towards the development of any-GK specific inhibitor have not yielded any successful results. The popular inhibitor in use is glycerol, at a concentration of 5 mM and above (*20*). This concentration is physiologically high and clinically impracticable.

After identification of a target enzyme, knowledge of its properties becomes the initial step towards identification of its inhibitor. Although the gene of GK (*gk*) from non-human parasites *T. b. brucei*, *Trypanosoma congolense* and *Trypanosoma vivax* have since been cloned and expressed (*11*, *14*, *16*), only preliminary kinetics data are available and may not be extrapolated to the GK of the human parasites (TbgGK and TbrGK). Notably, we already sequenced the *gk* from the TbgGK and TbrGK (GenBank database accession nos. AB517984 and AB517985, respectively), and a comparison of its product with that of the *gk* from the non-human infective *T. brucei* species (TREU927; accession no. XM_822408) revealed a single amino acid residue difference; phenylalanine at position 71 in *T. b. brucei* GK is changed to serine in the human parasites GK (*17*). The effect of such a residue difference on properties of the TbgGK and TbrGK remains unclear because kinetics and structural data of the parasites GK are unavailable. In addition, although the crystals of TbgGK showing ~2.7 Å resolution have been obtained (*17*), efforts towards improving the resolution beyond the 2.7 Å resolution repeatedly failed because of unstable nature of TbgGK. For drug design, a crystal structure should be solved at better than 2.3 Å resolution. Together, these impose the need for further studies on the purification and enzymology of human trypanosome GK.

Here, we optimized the protocol of obtaining higher yield of a highly active overproduced GK of human trypanosomes, purified it further and examined its kinetic and thermodynamic properties. Furthermore, a condition for maintaining the enzyme stability was found after which high-resolution crystals of the GK were obtained.

Materials and Methods

Bacterial strains, plasmids and reagents

One Shot Top10 chemically competent *Escherichia coli* (Invitrogen) was used as the host strain for propagation and maintenance of *gk*-cloned plasmids, whereas JM109 (DE3 + pRARE2) *E. coli* (Novagen) was used as host strain for protein expression. The plasmid pET151/D-TOPO (Invitrogen) was used as a cloning vector for *gk*. This vector contains an N-terminal tag coding sequence that adds a hexahistidinyl-tag (His-tag) to the N-terminal end of the expressed GK. MagExtractor kit for plasmid purification, gel extraction and PCR product purification kits were purchased from TOYOBO, Japan. Ni-NTA affinity resin was obtained from Qiagen (Germany). All other reagents were of the highest grade available and obtained from Sigma (USA) or WAKO (Japan).

Plasmid construction for recombinant GK expression

Prepared cDNA library from stocks of BSFs *T. b. gambiense* (IL2343), as previously described in Balogun *et al.* (*17*), was used as templates for the amplification of *gk* using 5′-CACCATGAAGT ACGTCGGATCCATT-3′ and 5′-CTACAACTTTGCCCACTTCG TCCTC-3′ as sense and antisense cloning primers, respectively, using *PfuUltra* II Fusion HS DNA polymerase (Stratagene). Following the manufacturer's procedure, the blunt-ended gel-purified PCR product (*gk*) was inserted into pET151/D-TOPO plasmid vector (Invitrogen), and used for the chemical transformation of One Shot TOP10 *E. coli* cells. Transformants colonies were grown on 100 $\mu g\,ml^{-1}$ carbenicillin-supplemented Luria-Bertani (LB) plates. Construct-positive clones were confirmed by colony PCR and selected for liquid culture in LB media for vector construct amplification. Plasmids were extracted using TOYOBO MagExtractor kit, and subjected to further confirmation by digestion with NcoI. The correct construct was used to transform protein expression *E. coli* host. The construct-positive colonies were selected under carbenicillin and chloramphenicol pressure, and selected for storage and expression experiments. Expression of soluble and active GK was achieved by induction with 25 μM of the gratuitous inducer, isopropyl β-D-thiogalactopyranoside (IPTG) when optical density at 600 nm (OD_{600}) reached 0.5, and post-induction growth for 12 h at 20°C.

Optimized large-scale purification of GK

One hundred millilitre pre-culture from the transformant colony was prepared overnight and transferred into 10 l of LB medium supplemented with the above antibiotics at 100 and 34 $\mu g\,ml^{-1}$ concentration, respectively. The culture was grown in a batch bioreactor that was operated at 37°C, maximum aeration and agitated at 600 rpm in BIOFLO 2000 fermentor (New Brunswick Scientific, NJ, USA). The *E. coli* pellet was harvested by centrifugation at 10,000 × g, washed twice in 50 mM Tris–HCl buffer pH 7.6 containing 0.1 mM phenylmethylsolfonyl fluoride (PMSF) and resuspended in 140 ml of lysis buffer [100 mM phosphate buffer pH 6.8, 300 mM NaCl, 10 mM $MgSO_4$, 0.1 mM PMSF, 1 $mg\,ml^{-1}$ lysozyme and 10% (v/v) glycerol]. The proceeding procedure for purification of GK was basically as previously described (*17*). All purification steps were carried out at 4°C, and purity was assessed by SDS–PAGE (*18*).

SDS–*PAGE of GK*

Bacterial lysate, cytosolic fraction and peak fractions from Ni-NTA and Superdex 200 columns were subjected to discontinuous SDS–PAGE. The stacking and separating gels were 4% and 12% (w/v) acrylamide, respectively. Samples were mixed 1 : 1 (v:v) with 2× SDS–PAGE loading buffer [125 mM Tris–HCl, pH 6.8, 4% (w/v) SDS, 15.8% (v/v) glycerol, 0.2% (w/v) bromophenol blue (Nacalai tesque) and 10% (v/v) β-mercaptoethanol] and heated for 5 min at 95°C. Protein preparations were then loaded into wells of a 1.0-mm thick gel and run alongside a broad-ranged Precision Plus Protein Standards (Bio-Rad, Hercules, CA, USA) in 1× Tris-glycine running buffer [3.0 $g\,l^{-1}$ Trizma-base, 14.3 $g\,l^{-1}$ glycine and 0.1% (w/v) SDS]. The gel was run at 20 Å per gel for 90 min and stained for 20 min in 0.2% Coomassie Brilliant Blue R, 50% (v/v) methanol and 10% (v/v) acetic acid and then de-stained in a solution containing 25% (v/v) methanol and 7.5% (v/v) acetic acid for 2 h. Gel documentation was done by scanning using colour imaging GT-7600U (Epson).

pH and temperature dependence of GK activity

Effects of pH on enzymatic activity were tested at 37°C (optimum temperature) over the pH range of 4–8. The reaction mixture composed of 1 mM EDTA, 5 mM $MgSO_4$, 0.5 mM $NADP^+$, 50 mM glucose, 2 mM ADP, 10 mM G3P and 1 unit each of hexokinase and glucose-6-phosphate dehydrogenase was incubated in the following buffers: 0.05 M acetate buffer pH 4.0–5.8; 0.1 M MOPS buffer pH 6.0–7.3 and 0.1 M Tris–HCl buffer pH 7.5–8.0. The temperature dependence of the purified enzyme was assessed over the range from 20 to 70°C in 0.1 M MOPS buffer pH 6.8 under optimum substrate concentrations. To deduce the thermodynamic parameter, activation energy (E_a) of the reaction, data for the activation region of the activity versus temperature curve were analysed using an

Arrhenius plot according to Eqs 1 and 2.

$$\ln(\text{spA}) = \ln A - \frac{E_a}{RT} \quad (1)$$

$$E_a = -\text{slope} \times R \quad (2)$$

where spA is specific activity (μmol min^{-1} mg^{-1}); A, Arrhenius constant for the reaction; R, gas constant (8.3145 J mol^{-1} K^{-1}) and T, temperature in K.

Assay and kinetics of rTbgGK

Reverse activity (G3P + ADP → glycerol + ATP) of TbgGK was measured at 37°C as previously described (*17*). Briefly, composition of the reaction mixture was as mentioned in 'pH and temperature dependence of GK activity' above. The ATP produced by TbgGK is utilized by hexokinase to generate glucose 6-phosphate from glucose, and finally glucose-6-phosphate dehydrogenase catalyses the production of NADPH from glucose 6-phosphate and $NADP^+$. The rate of NADPH accumulation was measured spectrophotometrically at 340 nm using the JASCO V-660 spectrophotometer. The kinetic parameters, K_m and V_{max} for ADP were determined at 12.5 mM constant concentration of G3P, while varying the concentration of ADP from 0.01 to 1.25 mM; the parameters were determined for G3P at 1.25 mM constant concentration of ADP over a concentration range of 0.1–12.5 mM of G3P.

Stability assessment and crystallization of TbgGK

For the stability studies, 5 mg ml^{-1} of protein in 100 mM sodium phosphate buffer pH 6.8 containing 100 mM NaCl was separately prepared to contain 5 mM ADP, 10 mM $MgSO_4$; and 5 mM ADP, 10 mM $MgSO_4$, 0.1% (v/v) glycerol; the control contained only 10 mM $MgSO_4$. They were all kept at 4°C and routinely checked for enzyme activity over a period of 4 weeks. Addition of 10 mM $MgSO_4$ and 0.1% (v/v) glycerol was crucial for the preservation of TbgGK activity. Using the stabilized enzyme, crystallization and X-ray diffraction data collection were carried out according to the methods described previously (*17*).

Results

Plasmid construction, expression and purification

The *gk* gene from African human trypanosomes coding for GK was directionally cloned into pET151/D-TOPO by a ligation-independent procedure. This was achieved by amplification of the gene with a primer set that were designed to ensure the gene contain extra CACC codon upstream of the initiation codon. The resulting construct was a 7.3-kb plasmid with two NcoI restriction sites, one in the His-tag region and the other in the insert. The insert was located downstream of sequences for T7 promoter and a fusion protein that contained the His-tag (Fig. 1a). Diagnosis for directionality of the insert was made by restriction digest using NcoI and confirmed by nucleotide sequencing (data not shown). Digestion with the restriction enzyme produced the expected 5.7 and 1.5 kb fragments (Fig. 1b).

The recombinant GK was expressed in JM109 (DE3 + pRARE2) with modified growth condition for optimum protein solubility. Expression of the soluble protein fused with N-terminal His_6-tag was achieved by growing the transformed *E. coli* at 20°C for 12 h after induction with 25 μM IPTG. At OD_{600} of 3.0, ~49 g wet cell pellet of the bacteria was harvested from 10 l culture. The cells were disrupted by passage through a French press that was operated at 140 MPa, and the lysate was fractionated by ultracentrifugation to obtain the cytosolic fraction containing the expressed soluble enzyme. The His_6-tagged 545 amino acid residues (60.4 kDa) enzyme was purified to homogeneity (Fig. 2) by a combination of Ni-NTA affinity chromatography and Superdex 200 gel filtration chromatography. Approximately, 150 mg of purified enzyme was obtained from a 10-l culture. This corresponds to 1.2% of the lysate's protein, and a purification fold of 75.2 (Table I). The protein eluted from the Superdex 200 column at a retention time corresponding to a molecular weight of ~119 kDa. The combination of sequence, gel exclusion chromatography and SDS–PAGE results suggests that the enzyme is functionally a homodimer. This accords with native GK obtained from the parasite's glycosomes, which was reported to be a dimer (*19*).

pH and temperature effects on activity of GK

Figure 3a shows the effect of pH on activity of the purified GK. The enzyme displayed an acidic to

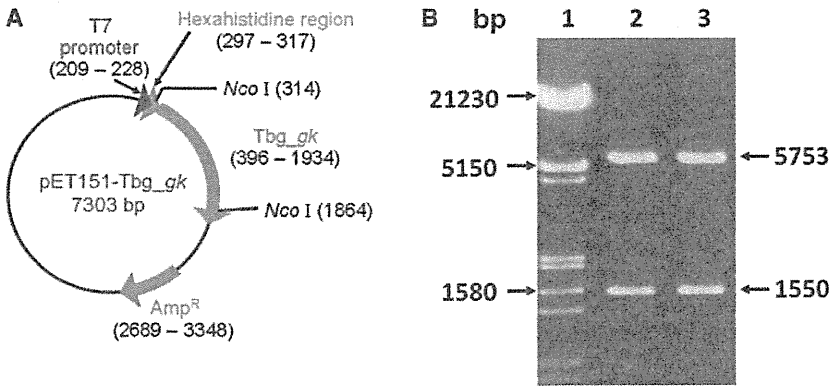

Fig. 1 Cloning and confirmation of *gk* in construct. (a) Summarized map of plasmid construct (Tbg or Tbr *gk*-pET151/D-TOPO) that was derived by a ligation-independent cloning of the genes into pET151/D-TOPO. The *gk* was amplified from cDNA libraries of the parasites. Arrows in the construct indicate the transcriptional direction. (b) The constructs were confirmed by digestion with NcoI to produce 5,753 and 1,550 bp nucleotide fragments. Lane 1 was loaded with 250 ng of marker 2 (Biorad), whereas lanes 2 and 3 were loaded with restriction reaction of constructs containing *gk* of Tbg and Tbr, respectively.

neutral property, showing an activity of 45–100% over a wide range of pH (5.0–7.0) measured at 37°C, with the optimum (100% activity) being pH 6.8. Activity was almost zero up to pH 4.5, but declined relatively slower in the alkaline side.

GK activity rose steadily with increase in reaction temperature over a range of 20–60°C. Arrhenius plot obtained from the temperature dependence study of trypanosome GK activity is shown in Fig. 3b. The E_a for the reaction was determined from the slope of a plot of ln (spA) versus $1/T$ via Eqs 1 and 2. As shown in Fig. 4, the E_a for the GK-catalysed G3P to ADP transphosphorylation was estimated to be 34.0 ± 0.31 kJ mol^{-1}. Also noteworthy is the coefficient of determination, R^2 value of 0.99 for the Arrhenius plot, which indicates that excellent agreement with the Arrhenius equation was observed between 25 and 50°C.

Kinetic analysis

The purified enzyme was highly active in both the forward and reverse directions. Under optimum conditions, the purified form exhibited a specific activity of ~32 μmol min^{-1} mg^{-1} for the reverse reaction. In the kinetic analysis, initial-velocity determinations for both reverse substrates ADP and G3P were carried out over wide concentration ranges. The data obtained were fitted for the Michaelis–Menten plot (Fig. 5a and b), which were transformed to double-reciprocal plots (Fig. 5a and b insets) for estimation of kinetic constants, K_m and V_{max}. While the values of these parameters for ADP were 0.9 mM and 25.3 μmol min^{-1} mg^{-1}, respectively, they were 5.5 mM and 20.0 μmol min^{-1} mg^{-1}, respectively, for G3P (Table II).

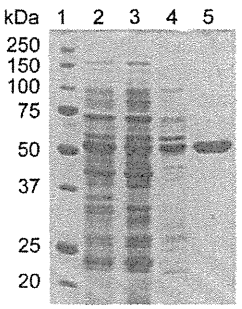

Fig. 2 Purity assessment of rTbgGK. 12.5% resolving SDS–PAGE gel stained with Coomasie Brilliant Blue R-250 showing purity levels of GK at the various purification steps. 1, molecular weight marker; 2, lysate of Tbg_*gk*-pET151/D-TOPO-transformed *E. coli* cells that were induced with 25 μM IPTG for rTbgGK expression; 3, cytosolic fraction; 4, pooled active fractions from affinity column and 5, gel chromatography fractions. Estimated molecular weight of this recombinant protein is 60 kDa, suggesting a dimer.

Stability and crystallization of TbgGK

The recombinant trypanosome GK was highly unstable. In 100 mM phosphate buffer pH 6.8, almost 50% of activity was lost in 1 week. After 4 weeks, only ~20% of activity was remaining. However, the presence of 5 mM ADP, 10 mM $MgSO_4$ and 0.1% (v/v) glycerol appeared to maintain the activity of GK intact over a period of 4 weeks (Fig. 6). This observation may be as a result of ADP and glycerol being GK ligands, might have occupied their respective binding sites, and helped to stabilize the enzyme. The same magnitude of instability was also observed for both the His-tagged enzyme and TEV protease-cleaved enzyme.

As an improvement on our previous crystals (*17*), the stabilized protein produced crystals diffracting X-ray to 1.9 Å resolution (Fig. 7). Analyses of the diffraction data revealed that these crystals of the TbgGK belong to a different space group ($P2_1$) from that of previous crystals ($P2_12_12_1$), and posses unit-cell parameters; $a = 62.16$, $b = 153.84$, $c = 120.10$ Å and $\beta = 89.95°$. The Matthews coefficient, V_M value was calculated to be 2.4 Å^3 Da^{-1} with an estimated solvent content of 48.2% (Matthews, 1968) when the presence of four TbgGK molecules (4 × 60.4 kDa) in the asymmetric unit was assumed. These values are slightly <2.5 Å^3 Da^{-1} and 50.4% observed for previous crystals, suggesting that the improvement of the resolution is achieved mainly by more compact packing of the stabilized TbgGK in the present crystals. In total, 554,224 observed reflections were recorded for the 180 images and were merged to 176,540 unique reflections from 50.0 to 1.90 Å resolution with an R_{merge} of 3.8%. Table III shows summary of the data collection and processing statistics.

Discussion

Although the importance of GK to the survival of African trypanosomes has since been chemically validated and recognized as a promising drug target (*20*, *21*), efforts towards obtaining high-resolution crystals of the enzyme necessary for the rational drug design, have been frustrated probably due to lack of

Table I. Purification table for rTbgGK.

Purification steps	Total activity (μmol min^{-1})	Total protein (mg)	Specific activity (μmol min^{-1} mg^{-1})	Activity recovery (%)	Purification (*x*-fold)
Lysate	5,360	12,730	0.4	100	1
Cytosol	5,320	10,000	0.5	99	1.3
Ni-NTA	4,630	210	22	86	52
Gel filtration	4,820	150	32	90	76

GK active fractions from Ni-NTA column were pooled, concentrated and gel purified on Superdex 200 to obtain purified form of the protein.

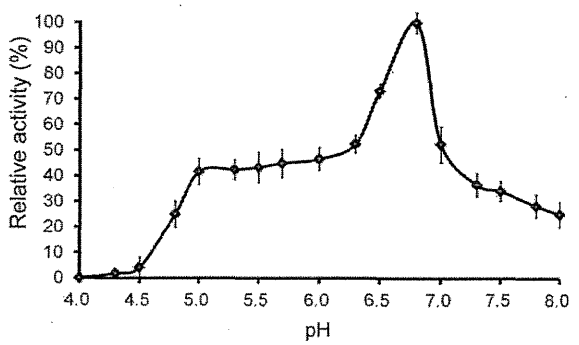

Fig. 3 pH profile of rTbgGK. Effect of pH on the GK activity was studied at 37°C, over a pH range of 4.0–8.0 in the following buffers: 50 mM acetate buffer pH 4.0–5.8; 100 mM MOPS buffer pH 6.0–7.3 and 0.1 M Tris–HCl buffer pH 7.5–8.0. 100% activity represents the specific activity at optimum pH, which correspond 32.15 μmol min^{-1} mg^{-1}. Values are means of duplicate determinations.

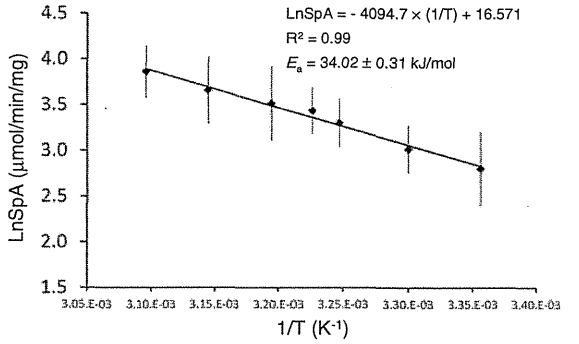

Fig. 4 E_a of trypanosome GK. Arrhenius plot showing the effect of temperature on the rate phosphoryl group transfer from G3P to ADP, determined at 25–50°C. The E_a value for the transfer is determined from slope of the best-fit line described by the Arrhenius equation, ln (specific activity) = $\ln A - [(E_a/R) \times (1/T)]$. Each data point plotted represents a mean of specific activity value for duplicate determinations at a given temperature.

adequate knowledge on its properties. Herein, we described how the gene coding the enzyme was optimally expressed and purified in large scale, report its kinetic and thermodynamic properties, and most importantly, found a condition to overcome its unstable nature.

The success of our ligation-independent plasmid construction (Fig. 1a) is shown by cleavability of the construct with NcoI endonuclease enzyme, as can be visualized by the two expected signals on 0.8% (w/v) agarose gel (Fig. 1b). Directional insertion of the inserted gene was achieved by engineering it to contain CACC overhang on its 5′ end. This was complimentarily attacked and annealed by a 3′-GTGG sequence overhang that was present in the pET-151/D-TOPO cloning/expression vector (*22*). In the vector, spacing between the ribosome-binding site and the translation initiation codon of the recombinant protein is seven nucleotides; this has been described to be optimum spacing for translation efficiency (*23*). An IPTG-inducible bacteriophage T7 promoter controls protein expression in this vector. The construct was transformed into several *E. coli* expression hosts but only JM109 (DE3 + pRARE2) could express the protein. The pRARE2 plasmids in this *E. coli* strain encode the tRNA genes that recognize the AGG, AGA, CGC, CGA, GGA, AUA, CUA and CCC rare codons (*24*). This implies the presence of rare codons in the gene of trypanosome GK. Indeed, there are 15 rare codons in the gene.

Maximal expression of the inserted gene was achieved by induction with 25 μM IPTG. In the uninduced transformants, GK expression was <1% of the amount in the induced culture. The full length recombinant protein was highly expressed. It migrated on the SDS–PAGE as the predicted 60 kDa protein (Fig. 2). We optimized for protein solubility by varying the transformants culture temperature after induction and found that reducing the temperature to 20°C and growing the bacteria for extended period (12 h), gave the best yield in terms of decrease in amount of inclusion body fraction and high-specific activity of the enzyme. Low temperature protein expression in *E. coli* slows down rate of protein translation, thereby reducing the hydrophobic interactions that may encourage protein misfolding, some of which may interact with one another and precipitate as inclusion bodies (*25*, *26*). The growth rate of the induced bacteria was three times faster in the fermentor for large scale culture as compared with the small scale culture in flasks. Doubling time for the transformants grown in 10 l culture in fermentor was 1 h, as compared with 3.2 h for 1 l culture at same temperature. This difference may be due to very high aeration and agitations supplied in the fermentor. Our purification protocol including large scale culture was reproducible. From 10 l culture, ~50 g wet cell pellet of the bacteria was obtained. The GK was well purified after the second chromatographic step, recovering almost 90% of the lysate activity and 152 mg of the pure protein (Fig. 2; Table I). Specific activity of the protein was very high, ~32 μmol min^{-1} mg^{-1} for the reverse direction, which is 3-fold the activity of GK purified from *T. b. brucei* that was earlier reported (*16*). This difference may be accounted for by the fact that we used an optimized temperature of 37°C for our enzyme assay; in previous reports 25°C was used.

The enzyme exhibited maximum activity at pH 6.8, but was also considerably active in the acidic region down to pH 5 (Fig. 3). This corresponds to what was reported for the GK of *T. b. brucei* (*16*). The enzyme was active at a temperature as high as 60°C, implying that the enzyme will still be beneficial to the parasites even when the infected animal develops hyperthermia, which is usually the case, the body temperature may rise to 40°C during infection (*27*). This temperature effect can be visualized by the lack of a break in the Arrhenius plot (Fig. 4), which is a proof that the enzyme conformation was not damaged over the temperature range between 25 and 60°C. The E_a of GK catalysed reaction was estimated as 34.0 ± 0.31 kJ mol^{-1} (Fig. 4), it is a measure of the energy

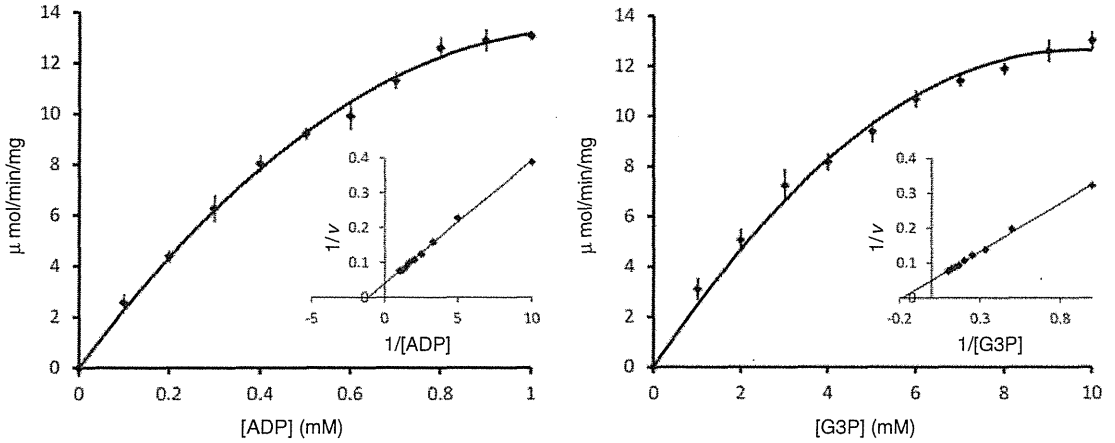

Fig. 5 Kinetic studies for human trypanosome GK. Specific activity data were fitted to Michaelis–Menten equation, which were transformed to double-reciprocal plots (inset panels) for determination of the kinetic parameters, summarized in Table II. (a) Determinations for ADP and (b) determinations for G3P. Results are means of duplicate experiments.

Table II. Kinetic parameters of rTbgGK for ADP and G3P.

Substrate	K_m (mM)	V_{max} (μmol min^{-1} mg^{-1})
ADP	0.90	25.3
G3P	5.54	20.0

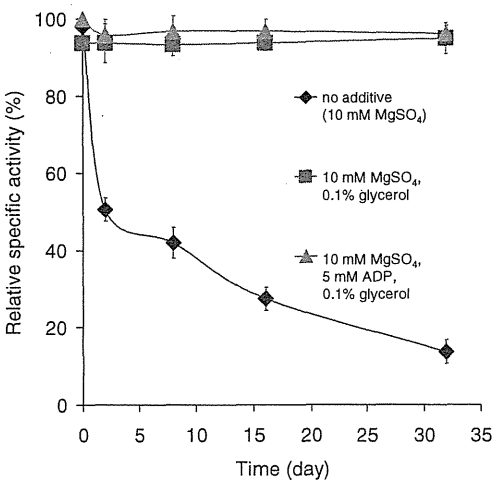

Fig. 6 Instability of TbgGK and its stabilized by the cofactor and substrates. The enzyme's function was optimally preserved for over 4 weeks by the presence of ligands (cube and triangle curves), as against loss of ~50% activity in just 48 h in the absence of these stabilizers (diamond curve). One hundred per cent activity represents the highest specific activity at day zero, which corresponds to 32.5 ± 0.7 μmol min^{-1} mg^{-1}. Values are means of duplicate determinations.

barrier that the reactants (G3P and ADP) must overcome before ATP and glycerol can be formed.

Kinetic constants for ADP and G3P were determined from the double-reciprocal plots obtained from initial velocity transformations (Fig. 5a and b inset). Their maximum velocity, V_{max} values were comparable, 25.3 and 20.0 μmol min^{-1} mg^{-1}, respectively, and values for their K_m were 0.9 and 5.5 mM, respectively (Fig. 5a and b). These values are in close agreement with the report on Gk of *T. b. brucei* with K_m values for ADP and G3P of 0.56 and 3.83 mM, respectively (*14*). From the K_m values, ADP binds more effectively to the enzyme active site, but G3P requires ~6-fold higher concentration than ADP to attain maximum velocity. This disparity in concentration as a result of their K_m values should be put in consideration when preparing the protein crystal complex of trypanosome GK with these substrates either by soaking or co-crystallization, for X-ray structural analysis.

Considering that the final goal of our study is to develop trypanosome-specific GK inhibitor(s) aimed for the rational design of anti-trypanosomal drug based on the X-ray structure of GK, unstable nature of the purified trypanosome GK was one of the important problems to be solved. The success of using X-ray crystallography for drug design is hinged on the ability to obtain crystals of the target molecule that can diffract X-ray to a resolution of better than 2.3 Å at which atomic and molecular fragments are more easily recognized (*28*). We have since succeeded at obtaining the initial crystals of the protein diffracting X-rays to ~2.8 Å (*17*). Efforts to improve the quality of the crystal have been difficult because rapid denaturation of the enzyme produces a mixture of active and inactive forms of TbgGK. Such non-uniformity is generally known to limit preparation of high-resolution crystals of proteins. To address this problem for TbgGK, a strategy to stabilize the protein (preserve its activity) was necessary. Interestingly, the activity could be preserved by the addition of 0.1% (v/v) glycerol or a combination of 0.1% (v/v) glycerol plus 2 mM ADP in same buffer (Fig. 6). The additives (glycerol and ADP) are natural ligands of GK, which serve as a substrate for the forward and reverse reactions, respectively. Hence, stability was achieved when

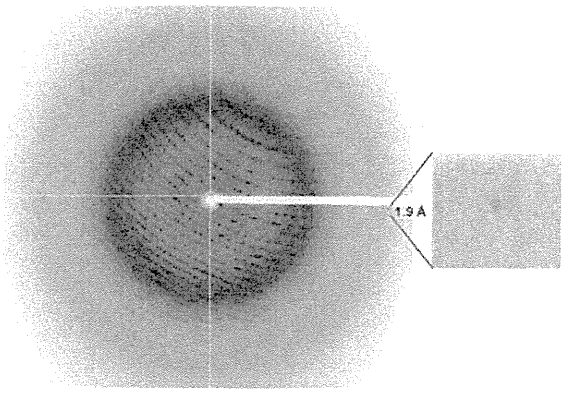

Fig. 7 A typical X-ray diffraction pattern of crystals obtained from the stabilized TbgGK. The detector edge corresponds to 1.8 Å resolution, and an enlarged image of the indicated area around 1.9 Å resolution is shown. The exposure time was 1 s with the oscillation angle of 1.0°.

Table III. Diffraction data statistics for crystal of TbgGK.

Space group	$P2_1$
Unit-cell parameters (Å)	$a=62.16$, $b=153.84$, $c=120.10$
Unit-cell parameters (°)	$\beta=89.95$
V_M[a] ($Å^3\,Da^{-1}$)	2.39
Solvent content[a] (%)	48.58
X-ray source	NW12 (PF)
Wavelength (Å)	1.000
Temperature (K)	100
Resolution (Å)	50–1.90 (1.93–1.90)
Total reflections	554,224
Unique reflections	176,540
Completeness (%)	92.3 (80.9)
R_{merge} I (%)[b]	3.8 (47.0)
I/σ	14.0 (3.1)

Values in parentheses are for the highest resolution shell.
[a]Assuming four molecules in the asymmetric unit.
[b]R_{merge} $(I)=\Sigma_{hkl}\ \Sigma_i|\ I_i(hkl)-\langle I(hkl)\rangle\ |/\Sigma_{hkl}\Sigma_i I_i(hkl)$, where $I_i(hkl)$ is the intensity of the ith observation of reflection hkl, and $\langle I(hkl)\rangle$ is their average.

the enzyme active site was probably occupied by the ligand(s). Furthermore, we found that the protein is soluble up to a concentration of 30 mg ml^{-1} in 0.1 M sodium phosphate buffer containing 10 mM Mg^{2+}, and remained 100% stable (constant specific activity) for more than 13 months when stored in 50% (v/v) glycerol at −80°C. This knowledge on the stability of TbgGK and the kinetics has enabled us to improve the resolution of TbgGK crystals to 1.9 Å (Fig. 7; Table III).

To conclude, we have optimized the procedure for high-level expression and large-scale purification of active human African trypanosome GK. This study also demonstrated the kinetic and thermodynamic parameters, which together with the knowledge of its stability will help improve our understanding of the enzyme properties, and accelerate efforts towards determining TbgGK structures complexed inhibitors at high accuracy. Detailed structure analyses and the molecular designs of specific inhibitors are ongoing.

Acknowledgements

This work was supported in part by Creative Scientific Research Grant 18GS0314 (to K.K.), Grant-in-aid for Scientific Research on Priority Areas 18073004 (to K.K.) and 19036010 (to S.H.) from the Japanese Society for the Promotion of Science, Targeted Proteins Research Program (to K.K. and S.H.) from the Japanese Ministry of Education, Science, Culture, Sports and Technology (MEXT), and by a grant to K.K. and S.H. from the Program for Promotion of Basic and Applied Researches for Innovations in Bio-oriented Industry (BRAIN). This work was also supported partly by JST/JICA, SATREPS (Science and Technology Research Partnership for Sustainable Development) (10000284) to K.K. E.O.B. was a MEXT scholar, and presently a postdoctoral fellow of the Japan Society for the Promotion of Science (JSPS).

Conflict of Interest: None declared.

References

1. Simarro, P.P., Jannin, J., and Cattand, P. (2008) Eliminating human African trypanosomiasis: where do we stand and what comes next? *PLoS Med.* **5**, e55
2. Brun, R., Blum, J., Chappuis, F., and Burri, C. (2009) Human African trypanosomiasis. *Lancet* **375**, 148–159
3. Delespaux, V. and de Koning, H.P. (2007) Drugs and drug resistance in African trypanosomiasis. *Drug Resist. Updat.* **10**, 30–50
4. Migchelsen, S.J., Buscher, P., Hoepelman, A.I., Schallig, H.D., and Adams, E.R. (2011) Human African trypanosomiasis: a review of non-endemic cases in the past 20 years. *Int. J. Infect. Dis.* **15**, e517–e524
5. Verlinde, C.L., Hannaert, V., Blonski, C., Willson, M., Perie, J.J., Fothergill-Gilmore, L.A., Opperdoes, F.R., Gelb, M.H., Hol, W.G., and Michels, P.A. (2001) Glycolysis as a target for the design of new anti-trypanosome drugs. *Drug Resist. Updat.* **4**, 50–65
6. Parsons, A.B., Brost, R.L., Ding, H., Li, Z., Zhang, C., Sheikh, B., Brown, G.W., Kane, P.M., Hughes, T.R., and Boone, C. (2004) Integration of chemical-genetic and genetic interaction data links bioactive compounds to cellular target pathways. *Nat. Biotechnol.* **22**, 62–69
7. Hannaert, V., Bringaud, F., Opperdoes, F.R., and Michels, P.A. (2003) Evolution of energy metabolism and its compartmentation in Kinetoplastida. *Kinetoplastid Biol. Dis.* **2**, 11
8. Haanstra, J.R., Kerkhoven, E.J., van Tuijl, A., Blits, M., Wurst, M., van Nuland, R., Albert, M.A., Michels, P.A., Bouwman, J., Clayton, C., Westerhoff, H.V., and Bakker, B.M. (2011) A domino effect in drug action: from metabolic assault towards parasite differentiation. *Mol. Microbiol.* **79**, 94–108
9. Gualdron-Lopez, M., Brennand, A., Avilan, L., and Michels, P.A. (2013) Translocation of solutes and proteins across the glycosomal membrane of trypanosomes; possibilities and limitations for targeting with trypanocidal drugs. *Parasitology* **140**, 1–20
10. Chaudhuri, M., Ott, R.D., and Hill, G.C. (2006) Trypanosome alternative oxidase: from molecule to function. *Trends Parasitol.* **22**, 484–491
11. Ohashi-Suzuki, M., Yabu, Y., Ohshima, S., Nakamura, K., Kido, Y., Sakamoto, K., Kita, K., Ohta, N., and Suzuki, T. (2011) Differential kinetic activities of glycerol kinase among African trypanosome species: phylogenetic and therapeutic implications. *J. Vet. Med. Sci.* **73**, 615–621
12. Saimoto, H., Kido, Y., Haga, Y., Sakamoto, K., and Kita, K. (2013) Pharmacophore identification of ascofuranone, a potent inhibitor of cyanide-insensitive

alternative oxidase of *Trypanosoma brucei*. *J. Biochem.* **153**, 267–273
13. Ajayi, W.U., Chaudhuri, M., and Hill, G.C. (2002) Site-directed mutagenesis reveals the essentiality of the conserved residues in the putative diiron active site of the trypanosome alternative oxidase. *J. Biol. Chem.* **277**, 8187–8193
14. Kralova, I., Rigden, D.J., Opperdoes, F.R., and Michels, P.A. (2000) Glycerol kinase of Trypanosoma brucei. Cloning, molecular characterization and mutagenesis. *Eur. J. Biochem.* **267**, 2323–2333
15. Bringaud, F., Riviere, L., and Coustou, V. (2006) Energy metabolism of trypanosomatids: adaptation to available carbon sources. *Mol. Biochem. Parasitol.* **149**, 1–9
16. Steinborn, K., Szallies, A., Mecke, D., and Duszenko, M. (2000) Cloning, heterologous expression and kinetic analysis of glycerol kinase (TbGLK1) from *Trypanosoma brucei*. *Biol. Chem.* **381**, 1071–1077
17. Balogun, E.O., Inaoka, D.K., Kido, Y., Shiba, T., Nara, T., Aoki, T., Honma, T., Tanaka, A., Inoue, M., Matsuoka, S., Michels, P.A., Harada, S., and Kita, K. (2010) Overproduction, purification, crystallization and preliminary X-ray diffraction analysis of *Trypanosoma brucei gambiense* glycerol kinase. *Acta Crystallogr. Sect. F Struct. Biol. Cryst. Commun.* **66**, 304–308
18. Laemmli, U.K. (1970) Cleavage of structural proteins during the assembly of the head of bacteriophage T4. *Nature* **227**, 680–685
19. Misset, O., Bos, O.J., and Opperdoes, F.R. (1986) Glycolytic enzymes of *Trypanosoma brucei*. Simultaneous purification, intraglycosomal concentrations and physical properties. *Eur. J. Biochem.* **157**, 441–453
20. Minagawa, N., Yabu, Y., Kita, K., Nagai, K., Ohta, N., Meguro, K., Sakajo, S., and Yoshimoto, A. (1997) An antibiotic, ascofuranone, specifically inhibits respiration and in vitro growth of long slender bloodstream forms of *Trypanosoma brucei brucei*. *Mol. Biochem. Parasitol.* **84**, 271–280
21. Yabu, Y., Suzuki, T., Nihei, C., Minagawa, N., Hosokawa, T., Nagai, K., Kita, K., and Ohta, N. (2006) Chemotherapeutic efficacy of ascofuranone in *Trypanosoma vivax*-infected mice without glycerol. *Parasitol. Int.* **55**, 39–43
22. Cheng, C. and Shuman, S. (2000) Recombinogenic flap ligation pathway for intrinsic repair of topoisomerase IB-induced double-strand breaks. *Mol. Cell. Biol.* **20**, 8059–8068
23. Chen, H., Bjerknes, M., Kumar, R., and Jay, E. (1994) Determination of the optimal aligned spacing between the Shine-Dalgarno sequence and the translation initiation codon of *Escherichia coli* mRNAs. *Nucleic Acids Res.* **22**, 4953–4957
24. Novy, R., Drott, D., Yaeger, K., and Mierenhof, R. (2001) Overcoming the codon bias of E. coli for enhanced protein expression. *inNovations* **12**, 1–3
25. Wickner, S., Maurizi, M.R., and Gottesman, S. (1999) Posttranslational quality control: folding, refolding, and degrading proteins. *Science* **286**, 1888–1893
26. Baneyx, F. and Mujacic, M. (2004) Recombinant protein folding and misfolding in *Escherichia coli*. *Nat. Biotechnol.* **22**, 1399–1408
27. Maina, N., Ngotho, J.M., Were, T., Thuita, J.K., Mwangangi, D.M., Kagira, J.M., Ndung'u, J.M., and Sternberg, J. (2004) Proinflammatory cytokine expression in the early phase of *Trypanosoma brucei rhodesiense* infection in vervet monkeys (*Cercopithecus aethiops*). *Infect. Immun.* **72**, 3063–3065
28. Blundell, T.L., Jhoti, H., and Abell, C. (2002) High-throughput crystallography for lead discovery in drug design. *Nat. Rev. Drug Discov.* **1**, 45–54

Mitochondrion 13 (2013) 602–609

Contents lists available at ScienceDirect

Mitochondrion

journal homepage: www.elsevier.com/locate/mito

Type II Fp of human mitochondrial respiratory complex II and its role in adaptation to hypoxia and nutrition-deprived conditions

Chika Sakai [a,1], Eriko Tomitsuka [a,2], Makoto Miyagishi [b], Shigeharu Harada [c], Kiyoshi Kita [a,*]

[a] Department of Biomedical Chemistry, Graduate School of Medicine, The University of Tokyo, Tokyo 113-0033, Japan
[b] Biomedical Research Institute, National Institute of Advanced Industrial Science and Technology, Ibaraki 305-8568, Japan
[c] Department of Applied Biology, Graduate School of Science and Technology, Kyoto Institute of Technology, Kyoto 606-8585, Japan

ARTICLE INFO

Article history:
Received 19 November 2012
received in revised form 8 August 2013
accepted 26 August 2013
Available online 2 September 2013

Keywords:
Human mitochondria
Complex II
Succinate-ubiquinone reductase
Flavoprotein
Fumarate respiration

ABSTRACT

The flavoprotein (Fp) subunit of human mitochondrial succinate-ubiquinone reductase (SQR, complex II) has isoforms (type I, type II). Type II Fp is predominantly expressed in some cancer and fetal tissues and those tissues are often exposed to ischemia. The present study shows that complex II with type II Fp has lower optimal pH than complex II with type I Fp, and type II Fp mRNA expression was induced by ischemia. The result suggests complex II with type II Fp may function in cells with low mitochondrial matrix pH caused by ischemia and its function is related to cellular adaptation to ischemia.

1. Introduction

Mitochondria play a central role in cellular energy metabolism in eukaryotes. The essential parts of oxidative metabolism are the tricarboxylic-acid (TCA) cycle, the respiratory chain and the adenosine tri-phosphate (ATP) synthesis machinery. The respiratory chain consists of four membrane-bound complexes within the mitochondrial inner membrane. Among these four complexes, succinate-ubiquinone reductase (SQR, complex II) is involved in the electron transport chain and the TCA cycle. Complex II catalyzes the oxidation of succinate to fumarate in the TCA cycle and transfers electrons to ubiquinone in the respiratory chain; thus, complex II is a direct link between the TCA cycle and respiratory chain. Mammalian complex II consists of four subunits. The flavoprotein (Fp, SDHA) subunit contains flavin adenine dinucleotide (FAD) as the prosthetic group, and the iron sulfur protein (Ip, SDHB) subunit contains three iron-sulfur clusters. Two hydrophobic cytochrome *b* (Cyb L, SDHC and Cyb S, SDHD) subunits function as the anchor subunits. The succinate binding site is located in the Fp subunit, while the quinone binding site consists of the Ip, Cyb L and CybS subunits (see recent review by Iverson et al., 2012).

Ip, Cyb L and Cyb S are considered to be tumor suppressors, and mutations in these subunits are associated with the development of pheochromocytoma and paraganglioma (Bayley et al., 2005; Baysal, 2003; Eng et al., 2003; Pollard et al., 2003; Rustin and Rotig, 2002; Selak et al., 2005). However, there is only one report showing Fp linked to tumorigenesis (Burnichon et al., 2010). This apparent lack of a direct link is probably due to the presence of two Fp isoforms (Briere et al., 2005; Rutter et al., 2010; Tomitsuka et al., 2003a). Mutations in Fp are linked to rare but severe metabolic disorders resulting from decreased activity of the TCA cycle and impaired oxidative phosphorylation. These autosomal recessive disorders are manifested as childhood encephalopathy, myopathy, adult optic atrophy, and Leigh syndrome (Bourgeron et al., 1995; Parfait et al., 2000; Van coster et al., 2003). Recently, it was reported that a significant amount of reactive oxygen species (ROS) was produced from complex II as well as complexes I and III, which are known for producing most of the ROS from the respiratory chain (Quinlan et al., 2012). This observation indicates that both wild-type complex II and mutant enzyme play an important role in diseases caused by ROS in addition to complexes I and III.

Recently, new proteins, SDHAF1 (succinate dehydrogenase complex assembly factor 1) and SDHAF2, were found as the first assembly factors of complex II (Ghezzi et al., 2009; Hao et al., 2009). Mutations in

Abbreviations: Fp, flavoprotein; SQR, succinate-ubiquinone reductase; SDHAF1, succinate-dehydrogenase assembly factor 1; SDHAF2, succinate-dehydrogenase assembly factor 2; SML, sucrose monolaurate; DCIP, 2,6-dichlorophenolindophenol; 3-NP, 3-nitropropionic acid; DTNB, 0.1 mM 5,5′-dithiobis-(2-nitrobenzoic acid); IC_{50}, 50% inhibitory concentration; HIF-1α, hypoxia-inducible factor-1α; QFR, quinol-fumarate reductase.

* Corresponding author at: Department of Biomedical Chemistry, Graduate School of Medicine, The University of Tokyo, Hongo, Bunkyo-ku, Tokyo 113-0033, Japan. Tel.: +81 3 5841 3526; fax: +81 3 5841 3444.
E-mail address: kitak@m.u-tokyo.ac.jp (K. Kita).
[1] Present address: Department of Mental Retardation and Birth Defect Research, National Institute of Neuroscience, National Center of Neurology and Psychiatry, Kodaira 187-8502, Japan.
[2] Present address: Department of Human Ecology, Graduate School of Medicine, The University of Tokyo, Tokyo 113-0033, Japan.

1567-7249/$ – see front matter © 2013 Elsevier B.V. and Mitochondria Research Society. All rights reserved.
http://dx.doi.org/10.1016/j.mito.2013.08.009

SDHAF1 might cause infantile leukoencephalopathy, and a mutation in SDHAF2 is linked to familial paraganglioma (Ghezzi et al., 2009; Hao et al., 2009).

In 2003, we identified two isoforms of human Fp, type I and type II (Tomitsuka et al., 2003a,b), which differ from each other only in two amino acid residues. Tyr 586 and Val 614 of type I Fp are replaced by Phe 586 and Ile 614 in type II Fp (numbered as 629 and 657 with N-terminal mitochondrial target sequences in the previous paper). Tyr 586 and Val 614 are well-conserved among mammalian Fps, and type II Fp is found only in human complex II. The type II Fp gene is not found in the NCBI database, and its location has not been clarified. The type I Fp gene is located on chromosome 5p15 and has an exon–intron structure (Tomitsuka et al., 2003a). Baysal et al. suggested that type II Fp is a variant of the Fp subunit that is explained by long-term balancing selection (Baysal et al., 2007).

The expression level of type I Fp mRNA is higher than that of type II Fp, although both isoforms were expressed in all organs tested (liver, heart, skeletal muscle, brain and kidney). The predominant expression of type I Fp was also shown in several cultured cell lines. However, some cancer cell lines showed a higher expression level of type II Fp mRNA than that of type I Fp (Sakai et al., 2012; Tomitsuka et al., 2003b). In addition, we found that some cancer tissues and fetal tissues also predominantly express type II Fp (Sakai et al., 2012).

The goal of the present study was to determine the biochemical properties of complex II with type II Fp. We constructed cell lines that suppress expression of type I Fp (type I Fp RNAi cells) or type II Fp (type II Fp RNAi cells) by RNA interference (RNAi) and characterized their complex IIs with each isoform. The complex II with type I Fp (complex II^{I}) mainly functions as SQR in mitochondria under normal conditions, and complex II with type II Fp (complex II^{II}) may function under conditions of relatively low pH in the mitochondrial matrix. Interestingly, we found that expression of type II Fp mRNA was increased in normal cells cultured under ischemic conditions.

2. Materials and methods

2.1. Cell culture

DLD-1 cells (Taiho Pharmaceutical Company, Japan) were cultured in RPMI-1640 (GIBCO BRL) supplemented with 10% (v/v) heat-inactivated fetal bovine serum (FBS, GIBCO BRL) under 5% CO_2 at 37 °C in a CO_2 incubator (ACI-165D, ASTEC). Human pancreatic stromal cells (DS Pharma Biomedical, Co., Ltd., Japan) were cultured in glucose-deprived medium (Sigma) supplemented with 3 g/L (17 mM) glucose, 10% FBS, and 4 mM glutamine (Sigma).

2.2. Construction of the siRNA expression plasmids

pcPUR + U6icassette (Miyagishi and Taira, 2002) was used for the siRNA expression vector. The shRNA sequences of the inserted in RNAi vectors against type I Fp and type II Fp were 5′-GTG TTT CGG TTC ATG GCT AAC GTG TGC TGT CCG TTA GTC ATG GAC CGA GAC AC-3′ and 5′-GTG TTT CGG TTG ATG GCT AAC GTG TGC TGT CCG TTA GTC ATC GAC CGA GAC AC-3′, respectively. (Target sequences for type I Fp and type II Fp are GTGTCTCGGTCCATGACTC and GTGTCTCGGTCGATGACTC, respectively). pcPUR + U6icassette was digested with BspMI, and the insert was ligated with a TaKaRa ligation kit according to the manufacturer's protocol. *E. coli* cells (TOP10 F′) were transformed by using the ligation mixture, and colonies were obtained. Plasmids were extracted from the cells grown from each colony, and nucleotide sequences of the plasmids were analyzed with ABI310 following the manufacturer's protocol.

2.3. Construction of Fp isoform-specific RNAi cells

Opti-MEM I (Invitrogen) was added to 0.5 μg of pcPUR + U6i cassette containing the short hairpin RNA sequence against each Fp isoform, brought to a final volume of 100 μL, and mixed gently. Then, 2 μL of Lipofectamine LTX (Invitrogen) was added, and the mixture was incubated for 25 min at room temperature. The plasmid solution (100 μL) and 500 μL of fresh medium were added to cells cultured in 24-well plates (BD Falcon). The cell cultures were subjected to gentle shaking and incubated for 48 h under 5% CO_2 at 37 °C. Forty-eight hours after transfection, 1/2 of the cells in confluent wells were transferred to 10-cm plates (BD Falcon). Following 6 h of incubation, puromycin (final concentration of 2, 3, or 6 μg/mL) was added, and drug selection was started. Puromycin was added every 3 days for 2 or 3 weeks until colonies reached a diameter of 3–5 mm. Then, colonies were isolated and transferred to 24-well plates. After 2 or 3 weeks, cells of the confluent wells were transferred to 10-cm plates for preparation of cell stock and 24-well plates for the extraction of RNA. Control cells were transfected with empty RNAi vector.

2.4. RNA extraction from cultured cells

RNA was extracted from cultured cells by using TRIzol reagent (Invitrogen) according to the manufacturer's protocol.

2.5. PCR-RFLP (restriction fragment length polymorphism) and mRNA expression pattern analysis of Fp isoforms

cDNA synthesis was performed according to the previously described method (9, 16). The cDNA was synthesized from 1 μg of total RNA after DNase I (Invitrogen) treatment by using oligo-dT primer by Rever Tra Ace (TOYOBO) at 42 °C for 1 h. Fp sequences were PCR amplified by using Taq DNA polymerase (TaKaRa) and an Fp primer set (sense primer, 5′-tggagacctaaagcacctga-3′; anti-sense primer, 5′-tcatcagtaggagcgaatgg-3′). PCR reactions were performed for 35 cycles with denaturation at 95 °C for 20 s, annealing at 55 °C for 20 s and extension at 72 °C for 1 min.

The amplified Fp PCR products were treated with AvaII (TaKaRa). One unit of AvaII was used for approximately 1 μg of PCR product. AvaII cuts the type I Fp PCR product at nucleotide 1680 of the cDNA sequence, but it does not cut type II Fp PCR product. AvaII-treated PCR products were analyzed by 1.5% (w/v) agarose gel electrophoresis including 1 × SYBR safe (Invitrogen). The intensity of the bands was calculated by NIH image software (National Institute of Health).

2.6. Mitochondria preparation

Preparation of mitochondria from cultured cells was performed as previously described (Tomitsuka et al., 2003a). Approximately 10^8 frozen cells were suspended in mitochondrial preparation buffer containing 250 mM sucrose, 20 mM HEPES, 3 mM EDTA and 1 mM malonate at pH 7.5. Cells were homogenized with a Potter-Elvehjem Teflon-pestle homogenizer (50 passes). The volume of the homogenate was adjusted to 10 mL by the addition of mitochondrial preparation buffer, and the mixture was centrifuged at 500 × *g* for 15 min at 4 °C to remove cell debris and nuclei. The supernatant was centrifuged at 14,300 × *g* for 15 min at 4 °C to precipitate the mitochondria. The pellet was resuspended in mitochondrial preparation buffer and centrifuged at 14,300 × g for 15 min at 4 °C. Finally, this pellet was suspended in mitochondrial preparation buffer without malonate for use as the mitochondrial fraction.

2.7. Two-dimensional electrophoresis (2-D electrophoresis) and Western blotting

The procedures were performed as previously described (Tomitsuka et al., 2003b). Mitochondria were solubilized with 2% (w/v) sucrose monolaurate (SML) and stirred for 1 h at 4 °C. After centrifugation at 200,000 × *g* for 1 h at 4 °C, the supernatant was analyzed by 2-D electrophoresis. For isoelectric point (p*I*) gel electrophoresis as the first dimension, a 7-cm Immobiline Dry Strip pH 3–10 (GE Healthcare) was used. After hydrating the gel strips, the solubilized samples (7 μL in total) containing 5% (v/v) glycerol, 0.5% (v/v) Ampholine, 0.6% (w/v) DTT, 1% (w/v) SML, and a trace amount of Orange G were applied to the gel strips. An IPG-phor isoelectric focusing unit (GE Healthcare) was used to apply 50 μA/strip at 500 V for 30 min, 1000 V for 30 min and 8000 V for 2 h on the step-n-hold mode. After electrophoresis, the strips were equilibrated with SDS-PAGE running buffer and further analyzed by SDS-PAGE as the second dimension.

SDS-PAGE was performed with 15% (w/v) polyacrylamide gels at 20 mA per 100 cm^2 gel. The separated proteins in the gel were transferred to nitrocellulose membranes (Schleicher & Schnell) for 1 h at 4 °C at 80 V in 25 mM Tris, 192 mM glycine and 20% (v/v) isopropyl alcohol. Transfer was performed in a buffer-tank-blotting apparatus. The membrane was incubated overnight at 4 °C with 1000-fold diluted anti-bovine Fp monoclonal antibody (Molecular Probes; 2E3) as the primary antibody in TBS (137 mM NaCl, 2.68 mM KCl and 25 mM Tris) containing 0.05% (v/v) Tween20 and 0.5% (w/v) skim milk. A 5000-fold dilution of anti-mouse IgG HRP (GE Healthcare) was used as the secondary antibody. Detection with ECL-plus was then performed according to the manufacturer's protocol (GE Healthcare), and the intensity of the bands was calculated by NIH image software.

2.8. Measurement of enzyme activities

SQR activity was measured in 50 mM potassium phosphate buffer (pH 7.5) by monitoring the absorbance change of 2,6-dichlorophenolindophenol (DCIP, Sigma) at 600 nm with an extinction coefficient of 21 mM^{-1} cm^{-1} for DCIP (Kler et al., 1991). For the optimal pH, SQR activity of complex II was examined in 50 mM potassium phosphate buffer with 0.1% (w/v) SML at different pH levels. For the inhibition assay, malonate (Wako), 3-nitropropionic acid (3-NP, Sigma) and oxaloacetate (Sigma) were used as the succinate binding site inhibitors of complex II, while atpenin A5 (Alexis Biochemicals) was used as the quinone binding site inhibitor.

Citrate synthase activity was measured in 100 mM Tris–HCl buffer (pH 8.0), 0.3 mM acetyl CoA (Sigma), 0.1 mM 5,5′-dithiobis-(2-nitrobenzoic acid) (DTNB). The reaction was started by the addition of 0.5 mM Oxaloacetate and liberation of free CoASH with DTNB was monitored at 412 nm by using the extinction coefficient of 13.6 mM^{-1} cm^{-1} for DTNB.

2.9. Cell culture under hypoxia and nutrition deprived conditions

For normal cell-culture, cells were incubated under 20% oxygen in medium containing 3 g/L (17 mM) glucose and 10% (v/v) FBS. For hypoxia and nutrition-deprived conditions, cells were incubated under 0.1% oxygen in glucose-free medium with or without 10% (v/v) FBS. For hypoxic cell-culture (0.1% oxygen), the Anaero Pack System was used (Mitsubishi Gas Chemical America, Inc., Japan).

3. Results

3.1. mRNA, protein expression of the Fp subunit and SQR activities in the RNAi cells

To characterize the biochemical properties of Fp isoforms, we constructed cell lines that stably express siRNA against one Fp isoform. Designing siRNA that distinguish single nucleotide difference is becoming general technique recent years (Schwarz et al., 2006; Takahashi et al., 2010; Yu et al., 2012). We investigated the biochemical features of complex IIs that contained the remaining Fp isoform by isolating the mitochondrial fractions from the siRNA-expressing cell lines. We previously characterized the biochemical properties of complex IIs from DLD-1 cells (Tomitsuka PhD thesis, 2003); therefore, we used DLD-1 cells in the present study. DLD-1 cell strains that suppress expression of type I Fp (type I Fp RNAi cells) or type II Fp (type II Fp RNAi cells) were obtained. The control cells were transfected with empty vector. In each type of RNAi cells, the mRNA expression of the targeted isoform was suppressed to less than 10% of the total Fp mRNA expression (Fig. 1).

The protein expression of both Fp isoforms (total Fp) per mitochondrion in the RNAi cells was examined by Western blotting. The intensity of the bands of total Fp was normalized to the band intensity of mitochondrial outer membrane protein, porin. Type I and type II Fp RNAi cells showed 59 ± 6.6% and 57 ± 14% of the total Fp expression in the control cells, respectively (Fig. 2A,B). Thus, the expression of total Fp protein per mitochondrion was suppressed by RNAi.

To detect each Fp isoform protein separately, we performed isoelectric focusing with the solubilized mitochondrial fraction from the RNAi cells. Complex II^{I} has an p*I* around 6–7, whereas complex II^{II} has a p*I* around 5–6 (Tomitsuka et al., 2003b). In Western blotting after the 2-D electrophoresis of type I Fp RNAi cells, about 94% of whole protein spots had a p*I* around 5–6, which corresponds to complex II^{II}. In contrast, 92% of all protein spots for type II Fp RNAi cells had a p*I* around 6–7, which corresponds to complex II^{I} (Fig. 3). This result allowed us to use the RNAi cells for biochemical studies of each isoform.

Enzyme activities of mitochondria were measured and normalized by citrate synthase activities. The relative SQR activity of type I Fp or type II Fp RNAi cells was 0.44 ± 0.02, 0.46 ± 0.1, respectively (Table 1) and it was 53 ± 9.1% and 48 ± 4.1% of control, in the same order. These enzyme activities were well correlated with the levels of total Fp protein expression in the cell lines. The values of the SQR activities divided by the Fp protein amount were almost the same in all cell lines (Fig. 2C). This result indicates that complex IIs with each Fp isoform had similar SQR molecular activities. As more than 90% of complex II in the mitochondria contained the Fp isoform that was not suppressed by RNAi, the mitochondrial fractions prepared from type I and type II Fp RNAi cells will be described as complex II^{II} and complex II^{I}, respectively.

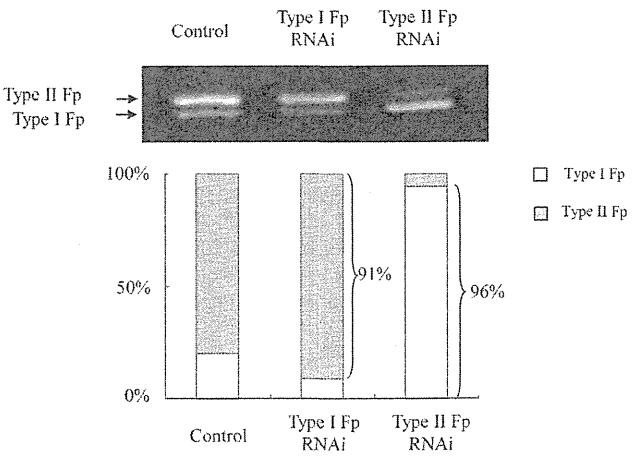

Fig. 1. mRNA expression patterns of the Fp isoforms in the RNAi cells. Amplified Fp RT-PCR products were digested with *Ava*II, which cuts only the type I Fp PCR product at one site (upper panel). The upper band is from the type II Fp PCR product, and the lower band is from the type I Fp PCR product. The intensity of the bands was calculated by NIH image software (National Institute of Health, lower panel). The white bar shows type I Fp, while the grey bar shows type II Fp.

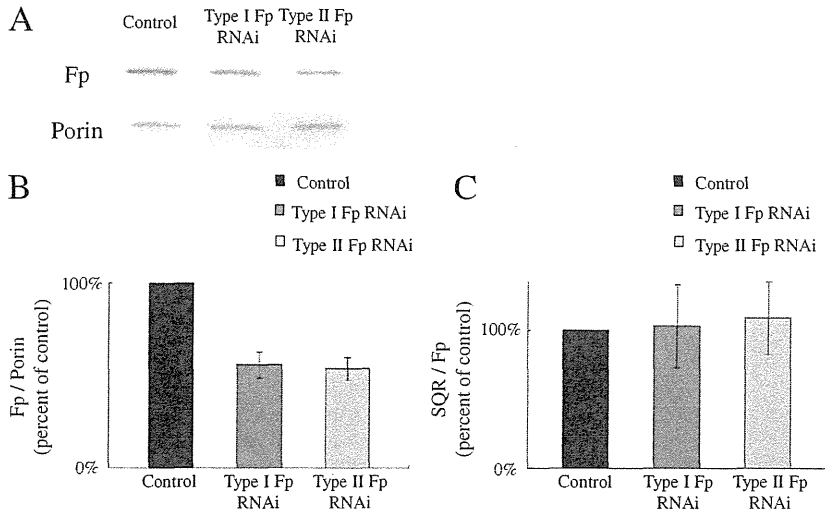

Fig. 2. Protein expression of Fp in the RNAi cells. Protein expression of Fp in the RNAi cells was examined by Western blotting (A) and normalized to the band intensity of mitochondrial porin (B). The values of SQR activities were divided by Fp protein (C). Intensity of the bands was calculated by NIH image software. Error bars show standard deviations above the means of three independent experiments.

3.2. Biochemical and kinetic properties of the two complex IIs with each isoform

To study the biochemical properties of complex IIs with each isoform, we performed a kinetic study and inhibition assay. We investigated the optimal pH of the complex IIs with each Fp isoform by analyzing SQR activities from pH 6.4 to pH 9.0. There was a difference between the two enzymes, with an optimum pH around 8.0 for complex II^{I} and 7.5 for complex II^{II} (Fig. 4). Moreover, the apparent K_m values for succinate were also different between each complex II. The apparent K_m values for succinate of complex II^{I} and complex II^{II} at pH 8.0, which is the optimal pH for complex II^{I}, were 210 ± 80 μM and 750 ± 140 μM, respectively. On the other hand, at pH 7.5, which is the optimal pH for complex II^{II}, the apparent K_m values for succinate of complex II^{I} and complex II^{II} were 860 ± 90 μM and 230 ± 70 μM, respectively. At pH 7.0, the apparent K_m values for succinate of complex II^{I} and complex II^{II} were 1100 ± 370 μM and 330 ± 90 μM, respectively (Table 2). These K_m values are within a range of reported succinate concentration in the cells in mice kidney (10 μM, Toma et al., 2008), rat liver (1 mM, Busch and Potter, 1952) and human brain (0.3 mM, Brockmann et al., 2002). In contrast to succinate, there was no clear difference in the apparent K_m values for ubiquinone-2 between complex IIs with each isoform at various pH values (Table 3). Thus, complex II^{II} has lower optimal pH than complex II^{I}, suggesting that complex II^{II} may function in cells that have a relatively low pH in the mitochondrial matrix.

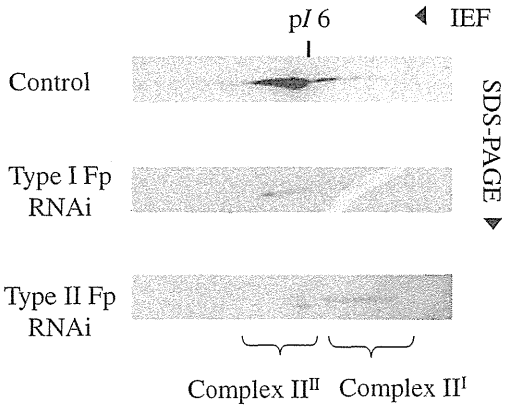

Fig. 3. Protein expression of the Fp isoforms in the RNAi cells. The mitochondria were solubilized, and the proteins were separated by 2-D electrophoresis, followed by Western blotting with anti-Fp antibody. Complex II^{I} has an isoelectric point (p*I*) around 6–7, whereas complex II^{II} has a p*I* around 5–6 (Tomitsuka et al., 2003b).

3.3. Inhibition of complex IIs with each isoform by specific inhibitors (oxaloacetate, malonate, 3-NP and atpenin A5)

To understand the biochemical features of complex IIs with each isoform, we studied their sensitivity to complex II-specific inhibitors. We used succinate binding site inhibitor 3-NP, which is a suicide inhibitor (Huang et al., 2006), as well as oxaloacetate and malonate, and a quinone binding-site inhibitor (atpenin A5) at pH 7.5 and pH 8.0 (Table 4). 3NP, oxaloacetate and malonate are structural analogs of succinate and inactivate complex II by binding to the succinate binding site (Huang et al., 2006). Under physiological conditions, oxaloacetate binds to complex II and regulates its activity (Ackrell et al., 1974). Atpenin A5 has been suggested to bind to a region that partly overlaps with the quinone binding site (Miyadera et al., 2003).

At both pH 7.5 and pH 8.0, the 50% inhibitory concentration (IC_{50}) of oxaloacetate for complex II^{I} was about two times lower than that for complex II^{II}. For malonate, the IC_{50} for complex II^{II} was about 1.6 times lower than that for complex II^{I} at pH 8.0, and the opposite tendency was observed at pH 7.5. Interestingly, for 3-NP, the inhibition curve of complex II^{II} was biphasic, while that of complex II^{I} was monophasic at pH 7.5. However, both curves were biphasic at pH 8.0 (Fig. 5). Differences in IC_{50} or inhibition patterns for succinate binding site inhibitors

Table 1
SQR activities of complex IIs with each isoform.

Assay	Specific activity (nmol/min/mg protein)		
	Control	Type I Fp RNAi	Type II Fp RNAi
SQR	79.7 ± 8.4	69.9 ± 5.3	54.3 ± 8.8
	(0.80 ± 0.08)[a]	(0.44 ± 0.02)[a]	(0.46 ± 0.1)[a]
Citrate synthase	100 ± 14	156 ± 17	119 ± 20

note: [a] normalized to citrate synthase activities.
Parentheses show SQR activities normalized to citrate synthase activities. Standard deviations were calculated from the results of three independent experiments.

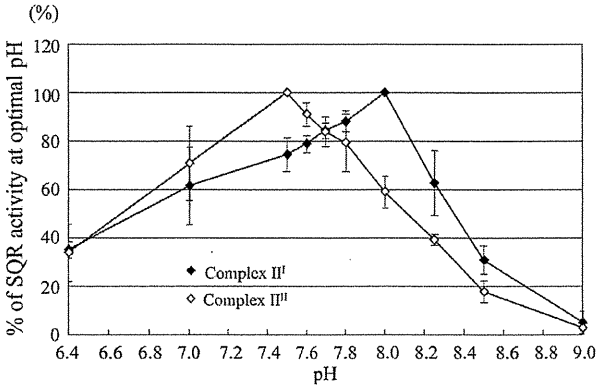

Fig. 4. Optimal pH for SQR activities of complex IIs with each isoform. SQR activities of the RNAi cells were determined at various pH levels. Filled diamonds, complex II^I; Open diamonds, complex II^{II}. The *y*-axis shows the ratio of SQR activity to activity at optimal pH for complex IIs with each isoform as 100%. The experiment was performed by using 50 mM potassium phosphate buffer pH 6.4, 7.0, 7.5, 7.6, 7.7, 7.8, 8.0, 8.25, 8.5 and 9.0. Error bars show two standard deviations above the means of three independent experiments.

between complex IIs with different isoforms suggest that the isoforms have structural differences in the active site of the enzymes.

3.4. Expression of Fp isoform mRNA under different cell-culture conditions

The physiological pH of mitochondrial matrix is around pH 8.0, which coincides with the optimal condition for complex II^I (Llopis et al., 1998). However, matrix pH drops when tissues are exposed to hypoxia and nutrition deprivation (Balut et al., 2008; Baron et al., 2005; Caplanusi et al., 2007). During hypoxia, mitochondrial pH drops from 8.0 to 7.0 – 7.2, which is almost the same as the cytosolic pH in adult rabbit cardiac myocytes (Ramshesh and Lemasters, 2012). The optimal pH for complex II^{II} was 7.5, suggesting that this isoform plays an important role during hypoxia and nutrition-deprived conditions.

To test this possibility, the effect of the culture conditions on the expression of type II Fp was studied. Under normal culture conditions (20% oxygen and medium containing 3 g/L (17 mM) glucose and 10% (v/v) FBS), type I Fp mRNA was predominantly expressed in human pancreatic stromal cells, and the type II Fp mRNA expression ratio was 4.2 ± 2.9%. When cells were cultured under hypoxia and nutrition-deprived conditions for 48 h, the expression ratio of type II Fp mRNA was increased. Cells cultured under hypoxia (0.1% oxygen) in glucose-free medium containing 10% FBS showed 9.1 ± 1.8% type II Fp mRNA expression. Furthermore, cells cultured under hypoxia (0.1% oxygen) and in glucose-free medium without FBS showed 13 ± 0.6% type II Fp mRNA expression (Fig. 6). These results clearly show that the expression of type II Fp mRNA increased in hypoxia and nutrition-deprived conditions, although the change in expression was relatively small.

4. Discussion

In recent years, it has become apparent that there exist several roles for respiratory complex II beyond metabolism. These include: succinate signaling, ROS generation, various disease states and aging. Moreover, it has a role in ischemic preconditioning and the function of the mitochondrial ATP-sensitive K^+ (mKATP) channel (Wojtovich et al., 2013). This work is focused on one new possibility of such diverse roles of complex II.

We performed detailed biochemical studies of complex II^{II}, which contains type II Fp as the catalytic subunit and found that complex II^{II} has different biochemical features from complex II^I, which is expressed in normal human tissues as the major complex II.

Complex IIs with each isoform had almost the same molecular activities (Fig. 2C). The possible physiological advantage of having two isoforms can be described as follows. If there are some mutations in one isoform, the other isoform can complement the defect of the mutant one. Mutations in subunits of complex II except Fp cause tumorigenesis. Possible causes of tumorigenesis are ROS production from mutated complex II (Hao et al., 2009; Ishii et al., 2007) or the accumulation of succinate as a result of SQR inhibition (Selak et al., 2005). Accumulated succinate inhibits hypoxia-inducible factor-1α (HIF-1α) prolyl hydroxylases in the cytosol, leading to the stabilization and activation of HIF-1α. Thus, succinate can increase the expression of genes that facilitate angiogenesis, metastasis, and glycolysis, ultimately leading to tumor progression. In addition to that, it has been recently revealed that there was vital connection between succinate metabolism and genomic DNA methylation during tumorigenesis (Killian et al., 2013). The expression of at least one of the two Fp isoforms presumably prohibits succinate accumulation in the presence of an Fp mutation (Briere et al., 2005; Rutter et al., 2010). This may be the reason why the mutation of the Fp subunit does not cause tumorigenesis like mutation of the other subunits.

The succinate binding site inhibitor showed different inhibition behaviors between complex IIs with each isoform, although there was no clear difference between isoforms in both inhibition patterns and IC_{50} by the quinone binding site inhibitor (Table 4). Since the different amino acid residues of each isoform are located in the Fp subunit, it is reasonable that they affect the succinate binding site but not the quinone binding site consisting of Ip and anchor subunits. Another important difference between isoforms was observed in the sensitivity to

Table 2
Apparent K_m values for succinate of complex IIs with each Fp isoform.

Fp	K_m (μM)			
	pH 7.0	pH 7.5	pH 7.8	pH 8.0
Type I Fp	1100 ± 370	860 ± 90	770 ± 120	210 ± 80
Type II Fp	330 ± 90	230 ± 70	240 ± 60	750 ± 140

The apparent K_m values for succinate of complex IIs with each isoform were estimated by SQR activity at pH 7.0, 7.5, 7.8 and pH 8.0. Standard deviations were calculated from the results of three independent experiments.

Table 3
Apparent K_m values for ubiquinone-2 of complex IIs with each Fp isoform.

Fp	K_m (μM)				
	pH 7.0	pH 7.5	pH 7.8	pH 8.0	pH 8.25
Type I Fp	2.5 (2.4, 2.5)	1.0 (1.3, 0.78)	0.94 (1.2, 0.67)	1.5 (1.6, 1.3)	8.0 (7.4, 8.5)
Type II Fp	1.8 (1.7, 1.8)	1.1 (1.2, 0.90)	0.91 (0.84, 0.98)	1.1 (1.2, 1.0)	5.8 (6.6, 5.0)

The apparent K_m values for ubiquinone-2 of complex IIs with each isoform were estimated by SQR activity at pH 7.0, 7.5, 7.8, 8.0 and pH 8.25. The values were averages calculated from the results of two independent experiments.

Table 4
IC_{50} of complex IIs with each isoform by various inhibitors.

Buffer pH	Fp	IC_{50}			
		Malonate (mM)	Oxaloacetate (μM)	3-NP (mM)	Atpenin A5 (nM)
7.5	I	0.14 ± 0.03	0.27 ± 0.10	3.8 ± 1.8	12 ± 1.1
	II	0.29 ± 0.06	0.55 ± 0.08	1.7 ± 0.2, 35 ± 6.1	9.1 ± 1.0
8.0	I	0.13 ± 0.02	0.27 ± 0.09	4.0 ± 1.4, 58 ± 13	25 ± 4.5
	II	0.08 ± 0.01	0.65 ± 0.08	2.6 ± 0.7, 46 ± 9.5	23 ± 6.5

3-NP: 3-nitropropionic acid.
Inhibition assay of complex IIs with each isoform by various inhibitors was performed at pH 7.5 and pH 8.0. Standard deviations were calculated from the results of three independent experiments.

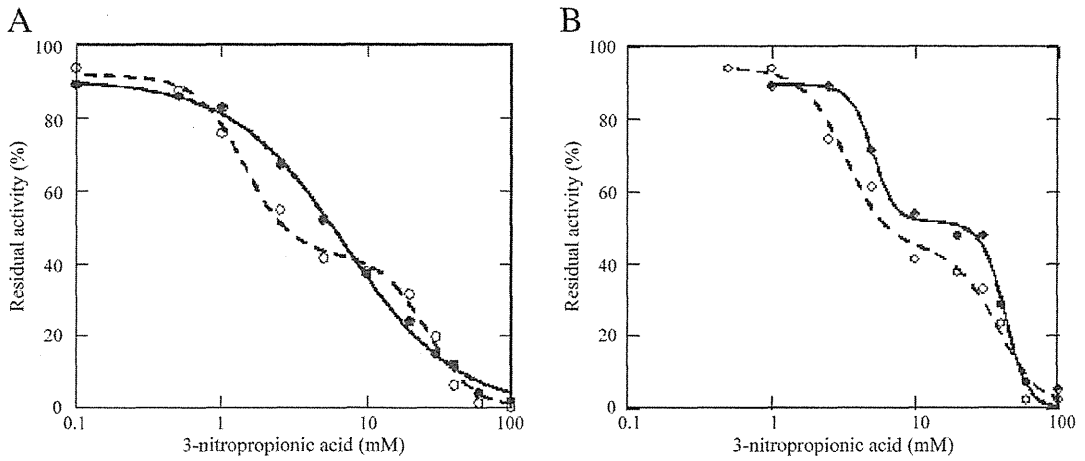

Fig. 5. Inhibition of complex IIs with each isoform by 3-nitropropionic acid (3-NP). Closed circles, complex II^{I}; Open circles, complex II^{II}. The *y-axis* shows the ratio of residual SQR activity to activity without 3-NP. (A) pH 7.5, 50 mM potassium phosphate buffer. (B) pH 8.0, 50 mM potassium phosphate buffer.

oxaloacetate. Complex II^{I} has two times more affinity to oxaloacetate at pH 7.5 and pH 8.0. Oxaloacetate is suggested to regulate complex II activity as a physiological inhibitor (Ackrell et al., 1974). It was suggested that oxaloacetate participates in the ischemic preconditioning by supporting a gradual activation of the respiratory chain from ischemia/reperfusion (Wojtovich et al., 2013). These differences in affinity to oxaloacetate of two Fp isoforms may have physiological meaning in the ischemic preconditioning.

The two amino acid residues that are different between the two Fp isoforms are located in the C-terminal domain. The Fp subunit consists of four subdomains: a large FAD-binding domain, a capping domain, a helical domain, and a C-terminal domain (Sun et al., 2005). The C-terminal domain is located almost at the surface of complex II, and the two amino acid residues that differ between the two isoforms are not likely to directly affect the succinate binding site. However, the differences between the predicted and estimated p*I* of complex IIs with each isoform as well as that of the kinetic properties indicate some differences in the active site of the two isoforms.

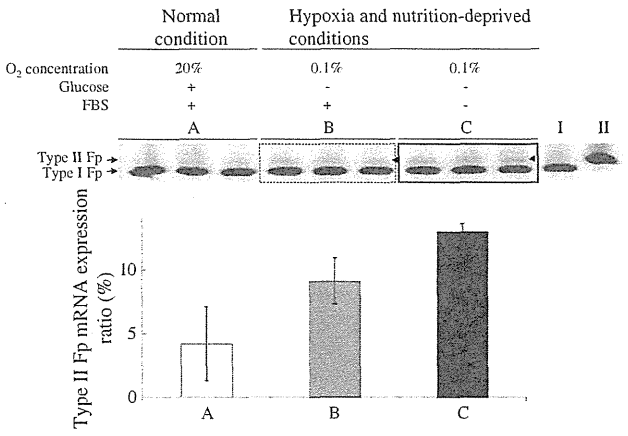

Fig. 6. Expression of Fp isoform mRNA under different cell-culture conditions. For the normal culture conditions, cells were incubated under 20% oxygen in medium containing 3 g/L (17 mM) glucose and 10% FBS. For hypoxia and nutrition-deprived conditions, cells were incubated under 0.1% oxygen in glucose-free medium with or without 10% FBS. After 48 h of incubation, total RNA was isolated from the cells, and mRNA expression analysis was performed. The lower panel shows the type II Fp mRNA expression ratio of cells cultured under different conditions. Error bars show the standard deviation from three independent experiments.

Complex II^{I} has a p*I* around 6–7, whereas complex II^{II} has a p*I* around 5–6, although the predicted p*I* values are the same (p*I* 5.87). One of the possible reasons why complex IIs with each isoform have different p*I* values is difference in the phosphorylation status. Several reports have suggested the existence of phosphorylation sites in the Fp subunit (Salvi et al., 2007; Tomitsuka et al., 2009). One of these sites, Tyr 500, is located close to Tyr 586, which is replaced by Phe 586 in type II Fp. Since the Tyr 586 Phe substitution will certainly destroy a hydrogen bond between Tyr 586 Oη and Glu 597 Oδ (3.13 Å), the local structure around Tyr 586 as well as the Tyr 500 phosphorylation status may be different between each isoform (Fig. 7). In fact, our recent study showed that the activity of human complex II was regulated by the phosphorylation of the enzyme (Tomitsuka et al., 2009, 2012). It should be noted that only the two amino acids substitution between the two Fp isoforms causes biochemical difference of complex IIs.

We identified several differences in the biochemical features and kinetic properties of the two Fp isoforms. Among these differences, the different optimal pH of each isoform has important physiological significance. The optimal pH for SQR activity of complex II^{I} is pH 8.0, whereas that of complex II^{II} is pH 7.5. The apparent K_m value for succinate of complex II^{I} was about four times lower than that of complex II^{II} at pH 8.0 (Table 2). The physiological pH of the mitochondria matrix is reported to be about 8.0 (Llopis et al., 1998); therefore, our results suggest that complex II^{I} mainly functions as SQR in mitochondria under normal conditions. This idea is consistent with the high expression level of type I Fp found in almost all organs and cultured cells (Sakai et al., 2012; Tomitsuka et al., 2003a,b). Although the optimal pH for complex IIs with each isoform are different, the apparent K_m values for succinate of complex IIs with each isoform were approximately the same at each optimal pH (Fig. 4, Table 2). Moreover, apparent K_m value for succinate of complex II^{II} is at least 3-fold lower than that of complex II^{I} between pH 7.0 and 7.8 (Table 2). These data indicate that complex II^{II} is more active when conditions in the mitochondrial matrix become relatively acidic, which occurs when the respiratory chain of cultured cells is poisoned by metabolic inhibitory substrate (Baron et al., 2005). A similar process to respiratory inhibition occurs in tissues under hypoxic conditions or ischemia (Balut et al., 2008; Baron et al., 2005; Caplanusi et al., 2007). As mentioned previously, the mitochondrial pH drops from 8.0 to 7.0–7.2 during hypoxia (Ramshesh and Lemasters, 2012). The increased expression of type II Fp mRNA under hypoxia and nutrition-deprived conditions (Fig. 6) indicates that type II Fp is induced under these conditions to maintain efficient respiration and an adequate energy supply. Hypoxia and nutrition-deprived conditions during embryogenesis and tumorigenesis are typical examples.